Derivation of weakly hydrodynamic models in the Dupuit-Forchheimer regime

Martin Parisot

Derivation of weakly hydrodynamic models in the Dupuit-Forchheimer regime

Martin Parisot*[1]

[1]Team CARDAMOM, Inria Bordeaux Sud-Ouest, 200 Avenue de la vieille tour, 33405 Talence cedex

March 31, 2024

Abstract

The current study is dedicated to the formal derivation of a hierarchic of asymptotic models that approximate the groundwater wave problem within the Dupuit-Forchheimer regime, over a regular, non-planar substratum. The derivation methodology employed bears resemblance to the techniques utilized in hierarchic of asymptotic models for approximating the water waves problem in the shallow water regime. Mathematically speaking, the asymptotic models manifest as nonlinear, non-local diffusion equations. We identify an energy dissipation law inherent to these models, thereby bolstering the physical validity and confidence in the proposed framework. A numerical strategy is proposed that preserved at the discrete level the energy dissipation. Several simulations are conducted to discuss and validate the dynamic behavior of the solution.

1 Introduction

The current study is dedicated to the formal derivation of a hierarchic of asymptotic models that approximate the groundwater wave problem within the Dupuit-Forchheimer regime, over a regular, non-planar substratum. The groundwater wave problem pertains to the mathematical representation of the phreatic water's evolution, with a specific focus on neglecting the unsaturated vadose zone dynamics over an unconfined aquifer. In recent years, the groundwater wave problem has garnered significant attention from both researchers and practicing engineers. This heightened interest can be attributed to various factors, notably climate change, increasing demands on water resources, pumping activities, and challenges related to saltwater intrusion in coastal regions. Mathematically, the groundwater wave problem is characterized as a three-dimensional free-surface problem, with flow dynamics

*martin.parisot@inria.fr

governed by Darcy's law. However, for applications on large spatial scales, direct numerical simulations of the groundwater wave problem often become computationally prohibitive. To circumvent these challenges, especially in the context of shallow aquifers, the groundwater wave problem can be effectively simplified through a vertically integrated modeling approach, leading to the Dupuit-Forchheimer model [12]. Despite its utility, the Dupuit-Forchheimer model exhibits limitations, particularly in scenarios where vertical velocities are non-negligible. This inadequacy becomes pronounced in the presence of drainage or injection processes [5, 33]. Additionally, the model's efficacy is compromised when confronted with steep bedrock slopes or boundary conditions mandating a significant slope for the water table.

To address these limitations, enhanced models have been introduced in the literature [9, 27, 35], which are formulated based on Hilbert expansions centered around the Dupuit-Forchheimer regime. While these refined models adeptly capture experimental outcomes for minor fluctuations in the groundwater wave, they exhibit deficiencies when confronted with more abrupt variations. Specifically, in such scenarios, the amplitude of high-frequency components escalates, and the energy of the model increase, see §3.3.4. Furthermore, it is pertinent to acknowledge several studies that have delineated analytical solutions, particularly in the context of stationary solutions [8, 20].

The foundation of this study rests upon recognizing the parallels between the groundwater wave problem and the water waves problem [22], as well as between the Dupuit-Forchheimer regime and the shallow water regime. The water waves model pertains to the mathematical representation of the evolution of a free-surface incompressible, irrotational, and inviscid fluid, governed by the Euler equations. This model is instrumental in describing phenomena such as river or coastal flows. In the context of shallow flows, the water waves problem can be effectively streamlined through a vertically integrated modeling approach, leading to the shallow water model [10]. To enhance the fidelity of wave propagation within this regime, a hierarchical series of models has been introduced [23]. In §3, our endeavor focuses on deriving analogous models for the Dupuit-Forchheimer regime. A salient advantage of these derived models, compared to the cited literature, resides in their mathematical structure. Specifically, these models adhere to an energy dissipation law, as shown in Proposition 2.

Mathematically speaking, the asymptotic models characterizing the Dupuit-Forchheimer regime are classified as nonlinear, non-local diffusion equations [7]. These models bear resemblance to various existing formulations present in the scientific literature. Notable analogues include the Patlak-Keller-Segel equations [18, 32], the Schurtz-Nicolai model [14, 15, 16, 29], the Stokes-Brinkman model [6, 21], and the non-local Exner model [3]. It is imperative to underscore that the computational analysis and numerical solution of these models pose significant challenges, as highlighted in the literature. In §4, we introduce a appropriate numerical strategy to describe the behavior of solutions of the new models. Importantly, this numerical approach ensures the preservation of energy dissipation at the discrete level, as shown in Proposition 5.

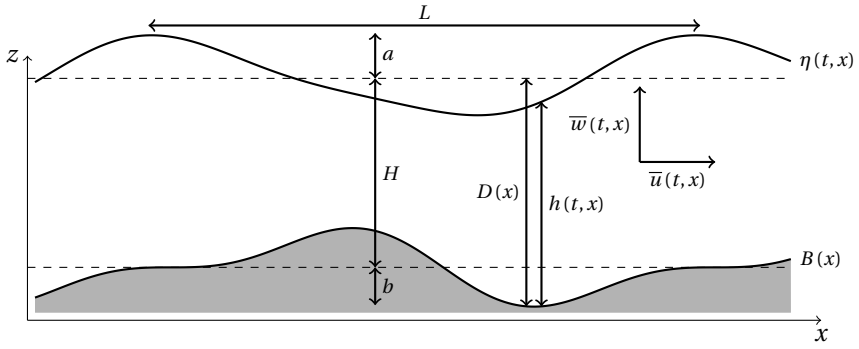

Figure 1: Illustration of model unknowns and characteristic lengths.

2 Hydrodynamic model in porous media

2.1 Governing equations

Consider a flow of an incompressible fluid within a porous medium. Let $S(x,z)$ denote the porosity of the porous medium, defined as the ratio of the volume of voids to the total volume within each elementary volume. Additionally, let $0 \le s(t,x,z) \le S(x,z)$ represent the fluid saturation, which is the ratio of the volume occupied by the fluid to the total volume within each elementary volume. The saturation $s(t,x,z)$ is governed by a conservation law, i.e.

$$\partial_t s + \nabla \cdot (su) + \partial_z (sw) = 0 \tag{1}$$

where $u(t,x,z) \in \mathbb{R}^d$ represents the horizontal fluid velocity, while $w(t,x,z) \in \mathbb{R}$ represents the vertical fluid velocity. We further postulate that the bottom boundary of the porous medium is characterized by a specified elevation function $B(x)$, commonly referred to as the bedrock where a non-penetration condition is enforced i.e.

$$u_{|_{z=B}} \cdot \nabla B - w_{|_{z=B}} = 0. \tag{2}$$

Within the porous medium, the fluid flow is governed by the Darcy's law, which establishes a relationship between the fluid velocity and the pressure field $p(t,x,z)$, i.e.

$$u = -\kappa \nabla p \qquad \text{and} \qquad w = -\kappa \left(\partial_z p + g\right) \tag{3}$$

with $\kappa(x,z) > 0$ represents the permeability of the porous medium, and g denotes the gravitational acceleration. One of the most challenging aspects of modeling fluid flow in porous media lies in accurately describing the pressure field p. In the present work, we focus on dynamics of the groundwater wave. We will see in the next section, under the assumption of predominantly horizontal flow, the pressure field becomes predominantly governed by the dynamics of the water table. This holds true even when considering the effects of weakly hydrodynamic terms.

2.2 Dynamics of the groundwater wave

In this study, our primary focus is directed towards the dynamics of the groundwater wave. We introduce an unknown elevation function, denoted as $\eta(t,x)$, which represents the water table. By definition, the flow under the water table is assumed to be saturated, i.e.

$$s(t,x,z) = \begin{cases} 0 & \text{, if } z > \eta(t,x), \\ S(x,z) & \text{, if } B(x) \le z \le \eta(t,x). \end{cases} \tag{4}$$

The water table satisfies a kinematic equation given by

$$\partial_t \eta + u_{|_{z=\eta}} \cdot \nabla \eta - w_{|_{z=\eta}} = 0. \tag{5}$$

Although it is beyond the scope of the current study, we mention here that considering the media above the water table as partially saturated in water would involve to add a source term in the kinematic equation. This source term encompasses both the water infiltration rate and the rising water attributed to capillary action.

As a consequence of (4), it is deduced that the subsurface flow beneath the water table adheres to a divergence-free condition, expressed as

$$\nabla \cdot (Su) + \partial_z (Sw) = 0. \tag{6}$$

By vertically integrating (1) from the bedrock to the water table, using Leibniz integral rules, and accounting for the non-penetration condition (2) and the kinematic equation (5), the evolution of the water table is obtained as

$$\partial_t V + \nabla \cdot \left(V \overline{u} \right) = 0 \tag{7}$$

where the water depth reads $h(t,x) = \eta(t,x) - B(x)$, the water volume by unit of surface given by

$$V(x,h) := \int_{B(x)}^{B(x)+h} S(x,z)\, \mathrm{d}z \ge 0$$

and the mean horizontal velocity defined by

$$\overline{u}(t,x) = \frac{1}{V(t,h(t,x))} \int_{B(x)}^{B(x)+h(t,x)} S(x,z)\, u(t,x,z)\, \mathrm{d}z$$

Alternatively, some may express (7) in its non-conservative form as

$$S_{|_{z=h+B}} \partial_t h + \nabla \cdot \left(\overline{S} h \overline{u} \right) = 0$$

where $\overline{S}$ denotes the mean porosity, defined as $\overline{S}(x,h) = \frac{V(x,h)}{h} \ge 0$.

Equations (3), (6), and (7) collectively formulate the model design as the groundwater wave problem. This problem bears notable resemblance to the well-established water waves problem [22], characterized by a conservation of mass beneath a free surface (7), a divergence-free condition (6), and an equation governing the 3D velocity (3). While a curl-free condition is introduced in the water waves problem, for

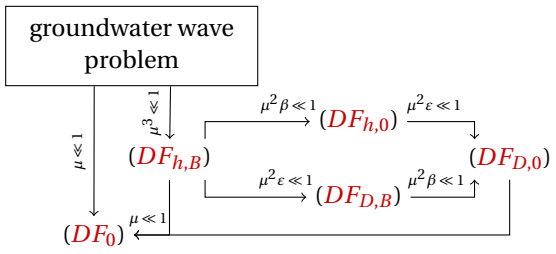

Figure 2: Scheme of the hierarchy of models in the Dupuit-Forchheimer regime.

the groundwater wave problem, it emerges as a consequence of Darcy's equation (3), specifically

$$\text{Curl}\left(\frac{1}{\kappa}\begin{pmatrix} u \\ w \end{pmatrix}\right) = 0. \tag{8}$$

The primary distinctions between the groundwater wave problem and the water waves problem lie in the spatial parameters κ and S. Analogous to the water waves problem, the groundwater wave problem poses significant computational challenges due to its three-dimensional nature and the presence of an unknown free-surface boundary. Such intricacy necessitates the derivation of simplified equation sets tailored to specific physical regimes, mimicking the approach adopted for the water waves problem in the shallow water regime. Subsequently, this study proceeds to close the model by approximating the mean horizontal velocity within the Dupuit-Forchheimer regime, wherein the vertical dimension is considerably smaller compared to the horizontal dimension.

3 Dupuit-Forchheimer regimes

We define the fundamental length scales characterizing the flow dynamics. Let H represents the characteristic water depth, L represents the characteristic horizontal length, a represents the mean amplitude of water table fluctuations, and b represents the mean amplitude of bedrock variations, as depicted in Figure 1. The primary dimensional scale for pressure is established by the hydrostatic pressure, expressed as $P = gH$. Leveraging the Darcy's law, it is inferred that the predominant velocity is given by $U = \frac{KgH}{L}$, where K represents the characteristic permeability value, while the characteristic timescale of the flow is defined as $T = \frac{L}{U} = \frac{L^2}{KgH}$. The dimensionless parameters associated with the shallowness of the flow, nonlinearity, and bedrock variations are denoted as $\mu = \frac{H}{L}$, $\epsilon = \frac{a}{H}$, and $\beta = \frac{b}{H}$, respectively. The Dupuit-Forchheimer regime is applicable to shallow flows over sufficiently flat bedrocks, characterized by $\mu \ll 1$. A graphical representation illustrating the hierarchical relationship between the subsequent models is provided in Figure 2.

3.1 The hydrostatic Dupuit-Forchheimer model

Let us start by presenting the well-known asymptotic hydrostatic Dupuit-Forchheimer model [12]. Utilizing the vertical component of Darcy's law (3), it becomes evident that the primary pressure aligns with the hydrostatic pressure, yielding

$$p = g\,(h + B - z) + O\big(\mu\big).$$

Substituting this outcome into the horizontal component of Darcy's law, it can be deduced that the horizontal velocity is dictated by the gradient of the water table

$$u = -g\kappa\nabla\,(h + B) + O\big(\mu\big)$$

This velocity is solely influenced by z through the permeability κ. By vertical integration, we obtain the hydrostatic Dupuit-Forchheimer model defined as

$$\partial_t V - \nabla\cdot\big(g\overline{\kappa}V\nabla(h+B)\big) = 0 \tag{DF_0}$$

with the effective permeability reads $\overline{\kappa}\,(x,h) := \frac{1}{V(x,h)}\int_{B(x)}^{B(x)+h} S\,(x,z)\,\kappa\,(x,z)\,\mathrm{d}z > 0$. This model serves as a $O\big(\mu\big)$-approximation of the groundwater wave model (3), (6), and (7).

We emphasize that the model (DF_0) adheres to an energy dissipation law. Specifically, by defining the energy as

$$\mathscr{E}\,(x,h) = g\int_{B(x)}^{B(x)+h} S\,(x,z)\,z\,\mathrm{d}z \tag{9}$$

we underscore the following established result.

Proposition 1. *Let h be solution of the hydrostatic Dupuit-Forchheimer model (DF_0). Then the potential energy (9) satisfies the following dissipation law*

$$\partial_t\mathscr{E} - \nabla\cdot\Big(g^2\overline{\kappa}\overline{S}h(h+B)\nabla(h+B)\Big) = -g^2\overline{\kappa}\overline{S}h\,|\nabla(h+B)|^2\,.$$

Proof. The derivative of the energy with respect to the water depth is given by:

$$\partial_h\mathscr{E}\,(x,h) = g\,(h+B)\,S_{|_{z=h+B}}$$

Multiplying (DF_0) by the potential $g\,(h+B)$, we obtain

$$\begin{aligned} 0 &= g\,(h+B)\Big(S_{|_{z=h+B}}\partial_t h - \nabla\cdot\Big(g\overline{\kappa}\overline{S}h\nabla\,(h+B)\Big)\Big) \\ &= \partial_t\mathscr{E} - \nabla\cdot\Big(g^2\overline{\kappa}\overline{S}h\,(h+B)\,\nabla\,(h+B)\Big) + g^2\overline{\kappa}\overline{S}h\,|\nabla\,(h+B)|^2 \end{aligned}$$

which confirms the previously stated result. □

3.2 Weakly hydrodynamics fully non-linear model

To enhance the accuracy of the models, we assume that the parameters characterizing the porous media, namely the porosity S and permeability κ, exhibit negligible variations in the vertical direction. Formally, this is expressed as $S(x,z) = \overline{S}(x)$ and $\kappa(x,z) = \overline{\kappa}(x)$. We introduce the hydrodynamic pressure as the deviation from the hydrostatic pressure, i.e.

$$q(t,x,z) = \frac{1}{\mu}\left(p(t,x,z) - g\left(\eta(t,x) - z\right)\right).$$

With this new variable, the Darcy law reads

$$u = -g\overline{\kappa}\nabla(h+B) - \mu\overline{\kappa}\nabla q \qquad \text{and} \qquad w = -\overline{\kappa}\partial_z q. \tag{10}$$

Also considering the flow regular enough, the horizontal velocity can be approximated as constant along the vertical direction, up to a perturbation of order $O(\mu)$. Formally:

$$u(t,x,z) = \overline{u}(x) + O\left(\mu\right).$$

Utilizing the divergence-free condition (6), we infer that the vertical velocity predominantly varies linearly with respect to the vertical coordinate. Incorporating the non-penetration condition (2), the vertical velocity reads

$$w(t,x,z) = w_{|_{z=B}} - \mu\frac{z-B}{\overline{S}}\nabla\cdot\left(\overline{S}\overline{u}\right) + O\left(\mu^2\right) = \mu\left(\beta\overline{u}\cdot\nabla B - \frac{z-B}{\overline{S}}\nabla\cdot\left(\overline{S}\overline{u}\right)\right) + O\left(\mu^2\right)$$

which can be decomposed into its vertically averaged and deviation components, $w(t,x,z) = \overline{w}(t,x) + \frac{z-B-\frac{h}{2}}{h}\widetilde{w}(t,x) + O\left(\mu^2\right)$ where

$$\overline{w} = \mu\left(\beta\overline{u}\cdot\nabla B - \frac{h}{2\overline{S}}\nabla\cdot\left(\overline{S}\overline{u}\right)\right) \qquad \text{and} \qquad \widetilde{w} = -\mu\frac{h}{\overline{S}}\nabla\cdot\left(\overline{S}\overline{u}\right). \tag{11}$$

With the vertical velocity from (10), we deduce that the hydrodynamic pressure exhibits primarily quadratic behavior with respect to the vertical coordinate

$$q(t,x,z) = \frac{B+h-z}{h}q_B + 3\frac{(z-B)(B+h-z)}{h^2}\left(2\overline{q} - q_B\right) + O\left(\mu^2\right)$$

where $\overline{q}(t,x) = \frac{1}{h(t,x)}\int_{B(x)}^{\eta(t,x)} q(t,x,z)dz$ represents the mean hydrodynamic pressure, and the hydrodynamic pressure at the bedrock is denoted as $q_B(t,x) = q(t,x,B(x))$. By construction, the hydrodynamic pressure vanishes at the water table, i.e., $q\left(t,x,\eta(t,x)\right) = 0$. A vertical integration and differentiation with respect to the vertical axis of the vertical velocity in (10) yield:

$$h\overline{w} = \overline{\kappa}q_B \qquad \text{and} \qquad h\widetilde{w} = 6\overline{\kappa}\left(2\overline{q} - q_B\right). \tag{12}$$

Using (11), we can express the hydrodynamic pressure as

$$\begin{aligned} q_B &= \mu\left(\beta\frac{h}{\overline{\kappa}}\overline{u}\cdot\nabla B - \frac{h^2}{2\overline{\kappa}\overline{S}}\nabla\cdot\left(\overline{S}\overline{u}\right)\right) \\ \text{and} \quad \overline{q} &= \mu\left(\beta\frac{h}{2\overline{\kappa}}\overline{u}\cdot\nabla B - \frac{h^2}{3\overline{\kappa}\overline{S}}\nabla\cdot\left(\overline{S}\overline{u}\right)\right) + O\left(\mu^2\right) \end{aligned} \tag{13}$$

By performing a vertical integration and applying the Leibniz integral rule, the mean horizontal velocity equation reads

$$h\overline{u} = -g\overline{\kappa}h\nabla(h+B) - \mu\overline{\kappa}\left(\nabla\left(h\overline{q}\right) + \beta q_B \nabla B\right). \tag{14}$$

Substituting (13) into (14), we obtain the weakly hydrodynamic fully non-linear Dupuit-Forchheimer model defined as

$$\partial_t V - \nabla\cdot\left(\overline{S}h\left(1+\mu^2\mathscr{T}_{h,B}\right)^{-1}\left(g\overline{\kappa}\nabla(h+B)\right)\right) = 0 \tag{$DF_{h,B}$}$$

where the operator $\mathscr{T}_{h,B}(U)$ is defined as

$$\mathscr{T}_{\mathbf{h},\mathbf{b}}(U) = \alpha_{\mathbf{b}}U + \frac{\overline{\kappa}}{\mathbf{h}}\nabla\left(\frac{\gamma_{\mathbf{h},\mathbf{b}}}{\overline{\kappa}}\cdot U\right) - \frac{\gamma_{\mathbf{h},\mathbf{b}}}{\overline{S}\mathbf{h}}\nabla\cdot\left(\overline{S}U\right) - \frac{\overline{\kappa}}{\mathbf{h}}\nabla\left(\frac{\omega_{\mathbf{h}}}{\overline{\kappa}\overline{S}}\nabla\cdot\left(\overline{S}U\right)\right) \tag{15}$$

$$\text{with}\quad \alpha_{\mathbf{b}} = \beta^2\nabla\mathbf{b}\otimes\nabla\mathbf{b}\,,\quad \gamma_{\mathbf{h},\mathbf{b}} = \beta\frac{\mathbf{h}^2}{2}\nabla\mathbf{b}\quad\text{and}\quad \omega_{\mathbf{h}} = \frac{\mathbf{h}^3}{3}\,,$$

This model serves as a $O\left(\mu^3\right)$-approximation of the groundwater wave model (3), (6), and (7).

We emphasize that the model ($DF_{h,B}$) adheres to an dissipation law of the energy (9) that for vertical constant parameters reads

$$\mathscr{E}(x,h) = g\overline{S}(x)\,h\left(\frac{h}{2}+B(x)\right) \tag{16}$$

we underscore the following established result.

Proposition 2. *Let h be solution of the weakly hydrodynamic fully non-linear Dupuit-Forchheimer model ($DF_{h,B}$). Then the potential energy (16) satisfies the following dissipation law*

$$\partial_t\mathscr{E} + \nabla\cdot\left(\left(g(h+B)+\mu\overline{q}\right)\overline{S}h\overline{u}\right) = -\frac{\overline{S}h}{\overline{\kappa}}\left(\left|\overline{u}\right|^2 + \overline{w}^2 + \frac{\widetilde{w}^2}{12}\right)$$

where the horizontal velocity, the vertical velocities and the hydrodynamics pressures are reconstructed from the water depth as $\overline{u}(x,h) = -g\left(1+\mu^2\mathscr{T}_{h,B}\right)^{-1}\left(\overline{\kappa}\nabla(h+B)\right)$, (11) and (12) respectively.

Proof. Multiplying ($DF_{h,B}$) by the potential $g(h+B)$, we obtain

$$\partial_t\mathscr{E} + \nabla\cdot\left(g(h+B)\,\overline{S}h\overline{u}\right) = g\overline{S}h\overline{u}\cdot\nabla(h+B)\,.$$

The right-hand side can be estimated by multiplying (14) by $\overline{u}$

$$g\overline{S}h\overline{u}\cdot\nabla(h+B) = -\frac{\overline{S}h\left|\overline{u}\right|^2}{\overline{\kappa}} - \mu\nabla\cdot\left(\overline{q}\overline{S}h\overline{u}\right) + \mu h\overline{q}\nabla\cdot\left(\overline{S}\overline{u}\right) - \mu\beta q_B\overline{S}\nabla B\cdot\overline{u}.$$

Similarly, by multiplying the two equations of (12) respectively by $\overline{w}$ and $\widetilde{w}$, we obtain

$$\frac{\overline{S}h\overline{w}^2}{\overline{\kappa}} = q_B\overline{S}\overline{w} \qquad \text{and} \qquad \frac{\overline{S}h\widetilde{w}^2}{\overline{\kappa}} = 6\overline{S}\left(2\overline{q}-q_B\right)\widetilde{w}$$

Summing up the last three relations, we obtain

$$\begin{aligned} g\overline{S}h\overline{u}\cdot\nabla\left(h+B\right) = &-\frac{\overline{S}h}{\overline{\kappa}}\left(\left|\overline{u}\right|^2+\overline{w}^2+\frac{\widetilde{w}^2}{12}\right)-\mu\nabla\cdot\left(\overline{S}h\overline{q}\overline{u}\right)\\ &+\overline{q}\left(\mu h\nabla\cdot\left(\overline{S}\overline{u}\right)+\overline{S}\widetilde{w}\right)-q_B\overline{S}\left(\mu\beta\nabla B\cdot\overline{u}-\overline{w}+\frac{\widetilde{w}}{2}\right). \end{aligned}$$

Given that the last two terms vanish due to (11), we can conclude the result. □

Remark 1. *The current study mainly concentrates on unbounded domains. However, it's noteworthy to observe that the natural boundary conditions of the hydrodynamic models are established on $\overline{u}$ (or $h\overline{u}$) rather than the water depth h. Physically, this corresponds to imposing the flux at the boundary. Simulating a fixed water depth at the boundary appears to be more intricate and is beyond the scope of this study.*

3.3 Simplified weakly hydrodynamics models

3.3.1 Fully non-linear small bedrock variation $\varepsilon = O(1)$ and $\beta = O(\mu)$

In scenarios where the variations in bedrock are small, i.e. $\beta \ll 1$, the model ($DF_{h,B}$) can be substantially simplified. Specifically, neglecting the terms in order of β, the weakly hydrodynamic fully non-linear Dupuit-Forchheimer model with small bedrock variations is expressed as

$$(DF_{h,0}) \qquad \partial_t V-\nabla\cdot\left(\overline{S}h\left(1+\mu^2\mathcal{T}_{h,0}\right)^{-1}\left(g\overline{\kappa}\nabla\left(h+B\right)\right)\right)=0$$

where the operator $\mathcal{T}_{\mathbf{h},0}(U)$ is defined as

$$\mathcal{T}_{\mathbf{h},0}(U) = -\frac{\overline{\kappa}}{\mathbf{h}}\nabla\left(\frac{\omega_{\mathbf{h}}}{\overline{\kappa}\overline{S}}\nabla\cdot\left(\overline{S}U\right)\right). \tag{17}$$

This model serves as a $O\left(\mu^2\beta,\mu^3\right)$-approximation of the groundwater wave model (3), (6), and (7).

We emphasize that the model ($DF_{h,0}$) adheres to an energy dissipation law.

Proposition 3. *Let h be solution of the weakly hydrodynamics fully non-linear model Dupuit-Forchheimer model with small bedrock variations ($DF_{h,0}$). Then the potential energy (16) satisfies the following dissipation law*

$$\partial_t\mathscr{E}+\nabla\cdot\left(\left(g\left(h+B\right)+\mu\overline{q}\right)\overline{S}h\overline{u}\right)=-\frac{\overline{S}h}{\overline{\kappa}}\left(\left|\overline{u}\right|^2+\frac{\widehat{w}^2}{3}\right)$$

where the horizontal velocity, the vertical velocities and the hydrodynamics pressures are reconstructed from the water depth as $\overline{u}(x,h) = -g\left(1+\mu^2\mathcal{T}_{h,B}\right)^{-1}\left(\overline{\kappa}\nabla\left(h+B\right)\right)$, $\widehat{w} = -\mu\frac{h}{\overline{S}}\nabla\cdot\left(\overline{S}\overline{u}\right)$ and $\overline{q} = \frac{h}{3\overline{\kappa}}\widehat{w}$.

Proof. The proof is similar to the proof of Proposition 2. □

3.3.2 Weakly non-linear large bedrock variation $\varepsilon = O(\mu)$ and $\beta = O(1)$

In scenarios where the variations in water table are small, i.e. $\varepsilon \ll 1$, the model ($DF_{h,B}$) can be substantially simplified. Specifically, the water depth can be advantageously replaced by the mean depth defined as $D(x) = H + B(x) - \int_\Omega B(x)\,\mathrm{d}x$, see Figure 1, the weakly hydrodynamic weakly non-linear Dupuit-Forchheimer model is expressed as

$$(DF_{D,B}) \qquad \partial_t V - \nabla \cdot \left(\overline{S} h \left(1 + \mathscr{T}_{D,B}\right)^{-1} \left(g \overline{\kappa} \nabla (h + B) \right) \right) = 0$$

where $\mathscr{T}_{\mathbf{h},\mathbf{b}}$ is defined in (15). This model serves as a $O(\mu^2\varepsilon, \mu^3)$-approximation of the groundwater wave model (3), (6), and (7).

The advantage of the weakly non-linear model ($DF_{D,B}$) is that the operator $\mathscr{T}_{D,B}$ remains independent of time, in contrast to the operator $\mathscr{T}_{h,B}$ in the model ($DF_{h,B}$). However, in practice, the numerical methods employed not fully exploit this time-independence, requiring additional time depend terms, see ($DF^{\mathrm{L}}_{D,0}$). Indeed, the weakly non-linear model ($DF_{D,B}$) come with two significant limitations, which have been previously discussed in the context of reduced models for water wave problems. Firstly, the energy dissipation properties observed in fully non-linear models, as described by Proposition 2 and Proposition 3, do not hold true for weakly non-linear models. Secondly, weakly non-linear models encounter issues at dry fronts, where the mean depth $D(x)$ approaches zero.

3.3.3 Weakly non-linear small bedrock variation $\varepsilon = O(\mu)$ and $\beta = O(\mu)$

In scenarios where both the variations in water table and the variations of bedrock are small, i.e. $\varepsilon \ll 1$ and $\beta \ll 1$, both simplifications can be carried out simultaneously. The weakly non-linear model on small bedrock defined as

$$(DF_{D,0}) \qquad \partial_t V - \nabla \cdot \left(\overline{S} h \left(1 + \mathscr{T}_{D,0}\right)^{-1} \left(g \overline{\kappa} \nabla (h + B) \right) \right) = 0$$

where $\mathscr{T}_{\mathbf{h},0}$ is defined in (17). This model serves as a $O(\mu^2\varepsilon, \mu^2\beta, \mu^3)$-approximation of the groundwater wave model (3), (6), and (7).

3.3.4 Approximation of the non-local operator by Taylor expansion

It is noteworthy that the inverses of the operators $\mathscr{T}_{h,B}(U)$ and $\mathscr{T}_{h,0}(U)$ can be approximated for small μ using Taylor expansion techniques, maintaining consistent modeling precision. Specifically, for the simplest weakly hydrodynamics fully non-linear Dupuit-Forchheimer model on small bedrock ($DF_{h,0}$), the inverse can be expressed as

$$\begin{aligned}\left(1 + \mu^2 \mathscr{T}_{h,0}\right)^{-1}(U) = U &+ \mu^2 \frac{\overline{\kappa}}{h} \nabla \left(\frac{\omega_h}{\overline{\kappa}\overline{S}} \nabla \cdot \left(\overline{S} U \right) \right) \\ &+ \mu^4 \frac{\overline{\kappa}}{h} \nabla \left(\frac{\omega_h}{\overline{\kappa}\overline{S}} \nabla \cdot \left(\frac{\overline{\kappa}\overline{S}}{h} \nabla \left(\frac{\omega_h}{\overline{\kappa}\overline{S}} \nabla \cdot \left(\overline{S} U \right) \right) \right) \right) + O\left(\mu^6\right).\end{aligned}$$

Truncated at order of μ^4, this reveals that the model introduced in [9, 27], defined by

$$\partial_t V - \nabla\cdot\left(g\overline{\kappa}\overline{S}\left(h\nabla(h+B)+\mu^2\nabla\left(\frac{\omega_h}{\overline{\kappa}\overline{S}}\nabla\cdot\left(\overline{\kappa}\overline{S}\nabla(h+B)\right)\right)\right)\right)=0. \tag{18}$$

This model serves as a $O\left(\mu^2\beta,\mu^3\right)$-approximation of the groundwater wave model (3), (6), and (7). Similarly, conducting the same computation with an arbitrary bedrock yields the model proposed in [35], which serves as a $O\left(\mu^3\right)$-approximation of the groundwater wave model (3), (6), and (7).

However, the Dagan model (18) exhibits instabilities at high frequencies. A detailed linear analysis is presented in §3.4. It's crucial to highlight that the energy (16) associated with solutions of the Dagan model (18) is not conserved. Instead, it follows the balance law

$$\partial_t\mathscr{E}-\nabla\cdot\left(g^2\overline{\kappa}\overline{S}\left(h^2\nabla h+\mu^2\left(h\nabla\left(\omega_h\Delta h\right)-\omega_h\Delta h\nabla h\right)\right)\right)=-g^2\overline{\kappa}\overline{S}\left(h\left|\nabla h\right|^2-\mu^2\omega_h\left|\Delta h\right|^2\right)$$

It's worth noting that this equation is not a dissipation law due to the absence of a sign on the right-hand side.

Expanding the non-local operator $\mathscr{T}_{h,B}$ to higher orders, up to μ^6-approximation, may potentially enhance the stability and well-posedness of the model without lost (neither gain) of approximation of the groundwater wave problem. Specifically the third order Dagan model can be defined as

$$\begin{aligned}\partial_t V &- \nabla\cdot\left(g\overline{\kappa}\overline{S}\left(h\nabla(h+B)+\mu^2\nabla\left(\frac{\omega_h}{\overline{\kappa}\overline{S}}\nabla\cdot\left(\overline{S}\overline{\kappa}\nabla(h+B)\right)\right)\right)\right)\\ &-\mu^4\nabla\cdot\left(g\overline{\kappa}\overline{S}\left(\nabla\left(\frac{\omega_h}{\overline{\kappa}\overline{S}}\nabla\cdot\left(\frac{\overline{\kappa}\overline{S}}{h}\nabla\left(\frac{\omega_h}{\overline{\kappa}\overline{S}}\nabla\cdot\left(\overline{S}\overline{\kappa}\nabla(h+B)\right)\right)\right)\right)\right)\right)=0\end{aligned} \tag{19}$$

Nonetheless, this approach presents significant computational challenges, as it involves the numerical approximation of exceedingly high derivatives. Furthermore, even with such an expanded form, the model would not satisfy an energy dissipation law.

3.4 Linear analysis and decay rates

In this section, we delve into the analysis of a linearized version of the Dupuit-Forchheimer models, specifically over a flat bottom. We consider constant parameters κ and S (hence $\overline{\kappa}$ and $\overline{S}$), and operate under the assumption of small amplitude water perturbation. Within this regime, we aim to estimate the decay of the linearized groundwater wave problem (3), (6), and (7), see §3.4.1. Additionally, we examine the decay rate of the asymptotic Dupuit-Forchheimer models, see §3.4.2. By comparing these decay rates, we can infer the domain of validity for each model. This analysis bears resemblance to the dispersion relation analysis employed in water wave problems [1]. Such dispersion relations have proven instrumental in comparing and evaluating the asymptotic shallow water models.

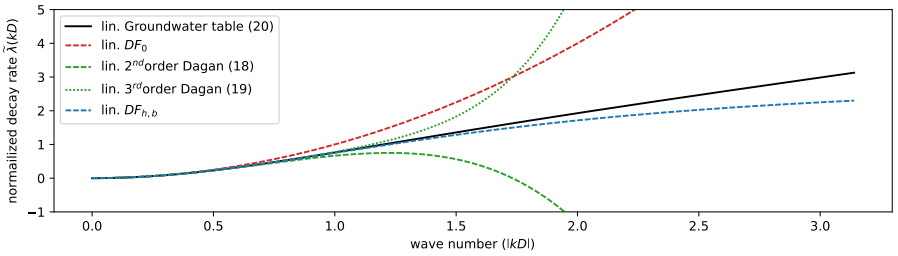

Figure 3: Decay rates corresponding to the linearized groundwater wave problem (20) (solid black line), to the hydrostatic model (DF_0) (dashed red line), to the linearized second order Dagan model (18) (dashed green line), to the linearized third order Dagan model (19) (dotted green line) and to the linearized hydrodynamic model ($DF_{h,B}$) (dashed blue line).

3.4.1 groundwater wave decay rate

Let us turn our attention to the linearized groundwater wave problem. As previously noted, Darcy's law dictates that the flow is irrotational, see (8). From this, we deduce the existence of a potential $\phi(t,x,z)$ such that $u(t,x,z) = \nabla\phi$ and $w(t,x,z) = \partial_z\phi$. The divergence-free condition (6) becomes $\Delta\phi + \partial_z^2\phi = 0$. At the free surface $z = \eta$, the kinematic equation (5) becomes $\partial_t\eta + \nabla\phi\cdot\nabla\eta - \partial_z\phi = 0$. The non-penetration equation over flat substratum (2) becomes $\partial_z\phi = 0$ at $z = -D$. The Darcy's law (3) imply that $\phi = -\kappa\left(p + gz\right)$. Upon linearizing around the state at rest $\left(\eta,\phi\right) = (0,0)$, the linearized groundwater wave problem is

$$\begin{aligned} \Delta\phi + \partial_z^2\phi &= 0\,, \\ \partial_z\phi &= 0\,, \qquad \text{at } z = -D \\ \partial_t\phi + g\overline{\kappa}\partial_z\phi &= 0\,, \qquad \text{at } z = 0. \end{aligned}$$

We seek solutions to the linearized model (3.4.1), assuming the form $\phi(t,x,z) = \Phi(z)\,e^{ik\cdot x}e^{-\lambda t}$, where k denotes the wave number and λ represents the decay rate. Utilizing the first two equations, we conventionally ascertain that the potential exponentially diminishes with depth. Specifically, the first equation leads to the differential relation $\Phi'' - |k|^2\Phi = 0$. Given the second equation, we deduce that $\Phi(z) = C\cosh(|k|(D+z))$, where C is a constant depending on the wave amplitude. Subsequently, the third equation results in the relation

$$\widetilde{\lambda}\left(|k|\,D\right) = |k|\,D\tanh\left(|k|\,D\right) \tag{20}$$

where we introduce the normalized decay rate $\widetilde{\lambda} = \frac{D}{g\overline{\kappa}}\lambda$.

3.4.2 Dupuit-Forchheimer decay rates

Now, considering the linearized Dupuit-Forchheimer models and seeking solutions of the form $\eta(t,x,z) = \eta^0 e^{ik\cdot x}e^{-\lambda t}$, we straightforwardly derive the decay rate as presented in Table 1.

	(DF_0)	(18)	(19)	$(DF_{h,B})$
$\widetilde{\lambda}$	$\lvert kD\rvert^2$	$\lvert kD\rvert^2 + \frac{\lvert kD\rvert^4}{3}$	$\lvert kD\rvert^2 + \frac{\lvert kD\rvert^4}{3} + \frac{\lvert kD\rvert^6}{9}$	$\frac{\lvert kD\rvert^2}{1+\frac{1}{3}\lvert kD\rvert^2}$

Table 1: Normalized decay rate of the Dupuit-Forchheimer models.

In Figure 3, the decay rates of each model are depicted. A significant difference in decay rates is observed at high frequencies among the models. Specifically, while high frequencies are damped extremely rapidly in the linearized hydrostatic model (DF_0), they undergo rapid amplification in the linearized Dagan model (18). Conversely, the high frequencies in the solution of the linearized hydrodynamic model ($DF_{h,B}$) are damped at a bounded rate. This observation emphases that the linearized hydrodynamic model described by Equation ($DF_{h,B}$) becomes ill-posed in the absence of assumptions concerning the regularity of the solution.

4 Numerical resolution

4.1 Numerical schemes and analysis

One of the primary applications of the Dupuit-Forchheimer model lies in estimating groundwater wave elevations for long-term scenarios, spanning periods of a year or even a decade. To carry out such simulations, it is imperative to employ an efficient numerical scheme devoid of time-step restrictions, which elucidates the prevalent adoption of implicit schemes for solving the hydrostatic Dupuit-Forchheimer equation (DF_0). The hydrodynamic Dupuit-Forchheimer models deviate from simple parabolic equations due to the non-local operator $\mathcal{T}_{\mathbf{h},\mathbf{b}}$. In this manuscript, our focus is solely on elementary boundary conditions, particularly the wall boundary condition $\overline{u}_{\partial\Omega}\cdot\mathfrak{n} = 0$ where $\mathfrak{n}$ denotes the normal to the computational domain boundary. A thorough investigation dedicated exclusively to boundary conditions for weakly hydrodynamic models seems essential, encompassing both continuous and discrete approaches, to provide an appropriate solution.

Let us narrow our description of the discretization tailored for the weakly dispersive fully non-linear model ($DF_{h,B}$). In our endeavor to devise an entropy satisfying scheme, see Proposition 5, we opt not to discretize the scalar form ($DF_{h,B}$) directly but rather its extended form encompassing (7), (10), (11), and (12). Moreover, to ensure robust performance in scenarios where hydrodynamic terms are negligible, our objective is to recover a conventional 3-points scheme as the parameter μ tends to zero. To achieve this, we introduce a staggered discretization approach. Dedicated schemes of ($DF_{h,0}$), ($DF_{D,B}$), ($DF_{D,0}$) and (DF_0) are presented next.

We consider a tessellation $\mathbb{T}$ of the horizontal domain $\Omega\subset\mathbb{R}^d$, comprising Card$(\mathbb{T})$ star-shaped control volumes. Let $k\in\mathbb{T}$ denote a control volume within the tessellation, $\mathbb{F}_k$ represent the set of its faces, and $\mathfrak{m}_k$ denote its surface area. Furthermore, for a given face f, its length is represented by $\mathfrak{m}_f$, and its neighboring control vol-

ume with respect to k is denoted by k_f, i.e. $k \cup k_f = f$. The unit normal pointing outwards from face f to control volume k is denoted by $\mathfrak{n}_k^{k_f}$. The collection of all faces is denoted by $\mathbb{F}$. We introduce the conventional centered discrete differential operators. For a vectorial data discretized at the faces, $V_\star = (V_f)_{f\in\mathbb{F}}$, the divergence on a primal cell $k \in \mathbb{T}$ is defined as

$$\nabla_k^\delta \cdot V_\star = \frac{1}{\mathfrak{m}_k} \sum_{f\in\mathbb{F}_k} V_f \cdot \mathfrak{n}_k^{k_f} \mathfrak{m}_f \tag{21}$$

For scalar data discretized across the cells, $\phi_\star = \left(\phi_k\right)_{k\in\mathbb{T}}$, the gradient in the vicinity of a face $f \in \mathbb{F}$ is defined as

$$\nabla_f^\delta \phi_\star = \frac{\phi_{k_f} - \phi_k}{\delta_f} \mathfrak{n}_k^{k_f}. \tag{22}$$

The characteristic length δ_f depends on the type of meshes employed. For instance, in 1D, $\delta_f = \frac{\mathfrak{m}_k + \mathfrak{m}_{k_f}}{2}$, while for 2D triangles, $\delta_f = \frac{\mathfrak{m}_k + \mathfrak{m}_{k_f}}{\sqrt{3}\mathfrak{m}_f}$. Note that these approximations assume the mesh to be relatively undistorted. For more general meshes, the use of advanced schemes, such as the DDFV discretization, becomes necessary, as discussed in [11, 17]. Furthermore, preserving the kernel of Grad-Div operators at the discrete level poses non-trivial challenges, as highlighted in [2].

We further introduce the following reconstructions. For scalar data discretized at the faces, $\psi_\star = \left(\psi_f\right)_{f\in\mathbb{F}}$, its reconstruction on a primal cell $k \in \mathbb{T}$ is defined as

$$\left[\psi_\star\right]_k = \frac{1}{\mathfrak{m}_k} \sum_{f\in\mathbb{F}_k} \psi_f \frac{\delta_f \mathfrak{m}_f}{2} \tag{23}$$

and for scalar data discretized across the cells, $\phi_\star = \left(\phi_k\right)_{k\in\mathbb{T}}$, its reconstruction at a face $f \in \mathbb{F}$ is given by

$$\left[\phi_\star\right]_f = \frac{\phi_{k_f} + \phi_k}{2}. \tag{24}$$

Lastly, time discretization is achieved using a time step δ_t, such that $t^{n+1} = t^n + \delta_t$.

Proposition 4. *The discrete operators* (21), (22), (23), *and* (24) *exhibit the following duality property, commonly referred to as the summation-by-part (SBP) property:*

$$\nabla_d \cdot ([\phi_\star]_\star V_\star) = [V_\star \cdot \nabla_d \phi_\star]_k + \phi_k \nabla_d \cdot V_\star. \tag{25}$$

Proof. Upon direct computation, we find

$$\begin{aligned}
\nabla_k^\delta \cdot \left(\left[\phi_\star\right]_\star V_\star\right) &= \frac{1}{\mathfrak{m}_k} \sum_{f\in\mathbb{F}_k} \frac{\phi_{k_f} + \phi_k}{2} V_f \cdot \mathfrak{n}_k^{k_f} \mathfrak{m}_f \\
&= \frac{1}{\mathfrak{m}_k} \sum_{f\in\mathbb{F}_k} V_f \cdot \frac{\phi_{k_f} - \phi_k}{\delta_f} \mathfrak{n}_k^{k_f} \frac{\delta_f}{2} \mathfrak{m}_f + \frac{\phi_k}{\mathfrak{m}_k} \sum_{f\in\mathbb{F}_k} V_f \cdot \mathfrak{n}_k^{k_f} \mathfrak{m}_f \\
&= \left[V_\star \cdot \nabla^\delta \phi_\star\right]_k + \phi_k \nabla_k^\delta \cdot V_\star.
\end{aligned}$$

□

4.1.1 Semi-implicite numerical scheme

For efficiency considerations, we propose a semi-implicit time scheme that necessitates only a singular resolution of the linear system per time step. This choice is deliberated in §4.1.2, where an alternative non-linear scheme is also introduced. Let us discretize the water depth and the bedrock on a primal mesh, denoted as h_k^n and B_k^n, that represent respectively the averaged water depth and the bedrock elevation within the control volume $k \in \mathbb{T}$ at time t^n. A straightforward discretization of (7) is given by

$$h_k^{n+1} = h_k^n - \frac{\delta_t}{\overline{S}_k} \nabla_k^\delta \cdot \left(\overline{S}_\star \left[h_\star^n \right]_\star \overline{u}_\star^{n+1} \right) \tag{26}$$

where $\overline{u}_f^{n+1}$ represents the approximation of the mean velocity $\overline{u}$ at the faces $f \in \mathbb{F}$ at time t^{n+1}. The porosity is discretized both at the cell level $\overline{S}_k$ and the face level $\overline{S}_f$ in the aforementioned formulae. However, it is plausible to consider one as a reconstruction from the other, for instance $\overline{S}_f = \left[\overline{S}_\star \right]_f$.

On the dual mesh, (14) is naturally discretized as

$$\begin{aligned} \left[h_\star^n \right]_f \overline{u}_f^{n+1} = &-g \overline{\kappa}_f \left[h_\star^n \right]_f \nabla_f^\delta \left(h_\star^{n+1} + B_\star \right) \\ &-\mu \overline{\kappa}_f \left(\nabla_f^\delta \left(h_\star^n \overline{q}_\star^{n+1} \right) + \beta \left[q_{B,\star}^{n+1} \right]_f \nabla_f^\delta B_\star \right) \end{aligned} \tag{27}$$

where $\overline{q}_k^{n+1}$ and $\overline{q}_{B,k}^{n+1}$ are respectively the approximations of the hydrodynamic pressure $\overline{q}$ and q_B on the control volume $k \in \mathbb{T}$ at time t^{n+1}. Similar to porosity, permeability is discretized at both cell levels $\overline{\kappa}_k$ and face levels $\overline{\kappa}_f$. However, it is plausible to consider one as a reconstruction from the other, for instance $\overline{\kappa}_k = \left[\overline{\kappa}_\star \right]_k$.

Equation (12) is naturally discretized on the primal mesh as

$$h_k^n \overline{w}_k^{n+1} = \overline{\kappa}_k q_{B,k}^{n+1} \qquad \text{and} \qquad h_k^n \widetilde{w}_k^{n+1} = 6 \overline{\kappa}_k \left(2 \overline{q}_k^{n+1} - q_{B,k}^{n+1} \right) \tag{28}$$

where $\overline{w}_k^{n+1}$ and $\widetilde{w}_k^{n+1}$ are respectively the approximations of the vertical velocities $\overline{w}$ and $\widetilde{w}$ on the control volume $k \in \mathbb{T}$ at time t^{n+1}.

Eventually the constraints (11) are discretized as

$$\begin{aligned} &\overline{S}_k \overline{w}_k^{n+1} = \mu \left(\beta \left[\overline{S}_\star \overline{u}_\star^{n+1} \cdot \nabla_\star^\delta B_\star \right]_k - \frac{h_k^n}{2} \nabla_k^\delta \cdot \left(\overline{S}_\star \overline{u}_\star^{n+1} \right) \right) \\ \text{and} \quad &\overline{S}_k \widetilde{w}_k^{n+1} = -\mu h_k^n \nabla_k^\delta \cdot \left(\overline{S}_\star \overline{u}_\star^{n+1} \right). \end{aligned} \tag{29}$$

To clarify the computation of the scheme (26), (27), (28), and (29), we can rewrite it in a form that closely mirrors the intended implementation. Starting with (29), substituting it into (28), and then into (27), we derive

$$\overline{u}_f^{n+1} + \mu^2 \mathcal{T}_{h_\star^n, B_\star}^f \left(\overline{u}_\star^{n+1} \right) = -g \overline{\kappa}_f \nabla_f^\delta \left(h_\star^{n+1} + B_\star \right)$$

where the discrete operator $\mathscr{T}^f_{h_\star,B_\star}$ is defined as

$$\begin{aligned}\mathscr{T}^f_{\mathbf{h}_\star,\mathbf{b}_\star}(V_\star) &= \beta^2\frac{\overline{\kappa}_f}{[\mathbf{h}_\star]_f}\left[\frac{\mathbf{h}_\star}{\overline{\kappa}_\star\overline{S}_\star}\left[\overline{S}_\star V_\star\cdot\nabla^\delta_\star\mathbf{b}_\star\right]_\star\right]_f\nabla^\delta_f\mathbf{b}_\star\\ &+\beta\frac{\overline{\kappa}_f}{[\mathbf{h}_\star]_f}\left(\nabla^\delta_f\left(\frac{|\mathbf{h}_\star|^2}{2\overline{\kappa}_\star\overline{S}_\star}\left[\overline{S}_\star V_\star\cdot\nabla^\delta_\star\mathbf{b}_\star\right]_\star\right)-\left[\frac{|\mathbf{h}_\star|^2}{2\overline{\kappa}_\star\overline{S}_\star}\nabla^\delta_\star\cdot\left(\overline{S}_\star V_\star\right)\right]_f\nabla^\delta_f\mathbf{b}_\star\right)\\ &-\frac{\overline{\kappa}_f}{[\mathbf{h}_\star]_f}\nabla^\delta_f\left(\frac{|\mathbf{h}_\star|^3}{3\overline{\kappa}_\star\overline{S}_\star}\nabla^\delta_\star\cdot\left(\overline{S}_\star V_\star\right)\right).\end{aligned}\tag{30}$$

Using (26), the initial step of the numerical scheme can be expressed as

$$\begin{aligned}\overline{u}^{n+1}_f+\mu^2\mathscr{T}^f_{h^n_\star,B_\star}\left(\overline{u}^{n+1}_\star\right)-g\overline{\kappa}_f\nabla^\delta_f\left(\frac{\delta_t}{\overline{S}_\star}\nabla^\delta_\star\cdot\left(\overline{S}_\star\left[h^n_\star\right]_\star\overline{u}^{n+1}_\star\right)\right)\\ =-g\overline{\kappa}_f\nabla^\delta_f\left(h^n_\star+B_\star\right)\end{aligned}\tag{$DF^{\mathrm{L}}_{h,B}$}$$

Subsequently, we explicitly compute the water depth $h^{n+1}_\star$ using (26). Note that only the normal component of the velocity $\overline{u}^{n+1}_f\cdot\mathrm{n}^{k_f}_k$ serves as a degree of freedom within the numerical scheme. This type of staggered grid, occasionally referred to as a MAC grid for Cartesian grids, finds extensive application in fluid dynamics, particularly in the diffusive or low-Mach regime [31, 34]. This is a consequence of the choice of the discrete gradient (22). However, this particular choice remains valid only for meshes that exhibit sufficient regularity, as discussed in [11, 17].

Note that the scheme ($DF^{\mathrm{L}}_{h,B}$) satisfies the steady state at rest condition $\nabla^\delta_f\left(h_\star+B_\star\right)=0$. Additionally, we emphasize its entropy-stability.

Proposition 5. *Let h^n_k be the solution of the numerical scheme ($DF^{\mathrm{L}}_{h,B}$). Then the discrete potential energy $\mathscr{E}_k(h)=g\overline{S}_k h\left(\frac{h}{2}+B_k\right)$ adheres to the following dissipation law*

$$\begin{aligned}\mathscr{E}_k\left(h^{n+1}_k\right)+\delta_t\nabla_k\cdot\left(\mathscr{G}^{n+1}_\star+\mathscr{H}^{n+1}_\star\right)\le\mathscr{E}_k\left(h^n_k\right)\\ -\delta_t\left(\left[\frac{\overline{S}_\star\left[h^n_\star\right]_\star}{\overline{\kappa}_\star}\left|\overline{u}^{n+1}_\star\right|^2\right]_k+\frac{\overline{S}_k h^n_k}{\overline{\kappa}_k}\left(\left|\overline{w}^{n+1}_k\right|^2+\frac{\left|\widetilde{w}^{n+1}_k\right|^2}{12}\right)\right)\end{aligned}$$

where the numerical energy flux is given by

$$\mathscr{G}^{n+1}_f=\left(g\left[h^n_\star\right]_f\left[h^{n+1}_\star+B_\star\right]_f+\mu\left[h^n_\star\overline{q}^{n+1}_\star\right]_f\right)\overline{S}_f\overline{u}^{n+1}_f$$

and the error in the numerical flux is

$$\mathscr{H}^{n+1}_f=\mu\beta\frac{\delta^2_f}{4}\overline{S}_f\overline{u}^{n+1}_f\cdot\nabla^\delta_f B_\star\nabla^\delta_f q^{n+1}_{B,\star}.$$

Proof. Here's the revised version of your provided text with improved English:

The proof closely follows the proof of Proposition 2. Multiplying (26) by $g\overline{S}_k\left(h^{n+1}_k+B_k\right)$ and using (25), we obtain

$$\begin{aligned}\mathscr{E}^{n+1}_k\le\mathscr{E}^n_k-\delta_t\nabla^\delta_k\cdot(g[h^n_\star]_\star[h^{n+1}_\star+B_\star]_\star\overline{S}_\star\overline{u}^{n+1}_\star)\\ +\delta_t g[\overline{S}_\star[h^n_\star]_\star\overline{u}^{n+1}_\star\cdot\nabla^\delta(h^{n+1}_\star+B_\star)]_k.\end{aligned}$$

Multiplying (27) by $\frac{\overline{S}_f}{\overline{\kappa}_f}\overline{u}_f^{n+1}$, we obtain

$$g\overline{S}_f\left[h_\star^n\right]_f\overline{u}_f^{n+1}\cdot\nabla_f^\delta\left(h_\star^{n+1}+B_\star\right)=-\frac{\overline{S}_f\left[h_\star^n\right]_f}{\overline{\kappa}_f}\left|\overline{u}_f^{n+1}\right|^2 \\ -\mu\overline{S}_f\overline{u}_f^{n+1}\cdot\left(\nabla_f^\delta\left(h_\star^n\overline{q}_\star^{n+1}\right)+\beta\left[q_{B,\star}^{n+1}\right]_f\nabla_f^\delta B_\star\right).$$

Computing the cell reconstruction of the above equation and using (25), we get

$$g\left[\overline{S}_\star\left[h_\star^n\right]_\star\overline{u}_\star^{n+1}\cdot\nabla_\star^\delta\left(h_\star^{n+1}+B_\star\right)\right]_k=-\left[\frac{\overline{S}_\star\left[h_\star^n\right]_\star}{\overline{\kappa}_\star}\left|\overline{u}_\star^{n+1}\right|^2\right]_k \\ -\mu\nabla_k^\delta\cdot\left(\left[h_\star^n\overline{q}_\star^{n+1}\right]_\star\overline{S}_\star\overline{u}_\star^{n+1}\right)+\mu h_k^n\overline{q}_k^{n+1}\nabla_k^\delta\cdot\left(\overline{S}_\star\overline{u}_\star^{n+1}\right) \\ -\mu\beta\left[\overline{S}_\star\left[q_{B,\star}^{n+1}\right]_\star\overline{u}_\star^{n+1}\cdot\nabla_\star^\delta B_\star\right]_k.$$

Focusing on the last term, we write

$$\begin{aligned}
&\left[\overline{S}_\star\left[q_{B,\star}^{n+1}\right]_\star\overline{u}_\star^{n+1}\cdot\nabla_\star^\delta B_\star\right]_k\\
&=\frac{1}{\mathfrak{m}_k}\sum_{f\in\mathbb{F}_k}\overline{S}_f\frac{q_{B,k_f}^{n+1}+q_{B,k}^{n+1}}{2}\overline{u}_f^{n+1}\cdot\nabla_f^\delta B_\star\frac{\delta_f\mathfrak{m}_f}{2}\\
&=\frac{q_{B,k}^{n+1}}{\mathfrak{m}_k}\sum_{f\in\mathbb{F}_k}\overline{S}_f\overline{u}_f^{n+1}\cdot\nabla_f^\delta B_\star\frac{\delta_f\mathfrak{m}_f}{2}+\frac{1}{\mathfrak{m}_k}\sum_{f\in\mathbb{F}_k}\overline{S}_f\frac{q_{B,k_f}^{n+1}-q_{B,k}^{n+1}}{\delta_f}\overline{u}_f^{n+1}\cdot\nabla_f^\delta B_\star\frac{\delta_f^2\mathfrak{m}_f}{4}\\
&=q_{B,k}^{n+1}\left[\overline{S}_\star\overline{u}_\star^{n+1}\cdot\nabla_\star^\delta B_\star\right]_k+\nabla_k^\delta\cdot\left(\frac{\delta_\star^2}{4}\overline{S}_\star\overline{u}_\star^{n+1}\cdot\nabla_\star^\delta B_\star\nabla_\star^\delta q_{B,\star}^{n+1}\right)\\
&=q_{B,k}^{n+1}\left[\overline{S}_\star\overline{u}_\star^{n+1}\cdot\nabla_\star^\delta B_\star\right]_k+\frac{1}{\mu\beta}\nabla_k^\delta\cdot\mathscr{H}_\star^{n+1}.
\end{aligned}$$

Similarly, multiplying the two equations of (28) by $\frac{\overline{S}_k}{\overline{\kappa}_k}\overline{w}_k^{n+1}$ and $\frac{\overline{S}_k}{\overline{\kappa}_k}\widetilde{w}_k^{n+1}$ respectively, we get

$$\frac{\overline{S}_k h_k^n}{\overline{\kappa}_k}\left|\overline{w}_k^{n+1}\right|^2=\overline{S}_k q_{B,k}^{n+1}\overline{w}_k^{n+1}$$
$$\text{and}\quad\frac{\overline{S}_k h_k^n}{\overline{\kappa}_k}\left|\widetilde{w}_k^{n+1}\right|^2=6\overline{S}_k\left(2\overline{q}_k^{n+1}-q_{B,k}^{n+1}\right)\widetilde{w}_k^{n+1}.$$

Combining all the equations, we conclude that the discrete energy is given by

$$\begin{aligned}
&\mathscr{E}_k^{n+1}+\delta_t\nabla_k^\delta\cdot\left(\mathscr{G}_\star^{n+1}+\mathscr{H}_\star^{n+1}\right)\\
&\quad=\mathscr{E}_k^n-\delta_t\left(\left[\frac{\overline{S}_\star\left[h_\star^n\right]_\star}{\overline{\kappa}_\star}\left|\overline{u}_\star^{n+1}\right|^2\right]_k+\frac{\overline{S}_k h_k^n}{\overline{\kappa}_k}\left(\left|\overline{w}_k^{n+1}\right|^2+\frac{\left|\widetilde{w}_k^{n+1}\right|^2}{12}\right)\right)\\
&\qquad+\delta_t\overline{q}_k^{n+1}\left(\mu h_k^n\nabla_k^\delta\cdot\left(\overline{S}_\star\overline{u}_\star^{n+1}\right)+\overline{S}_k\widetilde{w}_k^{n+1}\right)\\
&\qquad+\delta_t q_{B,k}^{n+1}\left(\overline{S}_k\left(\overline{w}_k^{n+1}-\frac{\widetilde{w}_k^{n+1}}{2}\right)-\mu\left[\overline{S}_\star\overline{u}_\star^{n+1}\cdot\nabla_\star^\delta B_\star\right]_k\right).
\end{aligned}$$

Using (29), the last two terms cancel out, leading us to conclude. □

The numerical flux $\mathscr{H}_f^{n+1}$ does not appear in the continuous energy balance Proposition 2. However, this term vanishes as the mesh size, particularly δ_f, tends to zero. Specifically, this term is of the order of δ_f^2, indicating that the scheme is second order in space. Nonetheless, due to the employment of a semi-implicit time scheme, the scheme remains first order in time.

- When $\mu^2\beta$ is negligible, the numerical scheme $(DF^{\mathrm{L}}_{h,B})$ tends to

$$(DF^{\mathrm{L}}_{h,0}) \qquad \begin{aligned} &\overline{u}_f^{n+1} + \mu^2 \mathscr{T}^f_{h_\star^n,0}\left(\overline{u}_\star^{n+1}\right) - g\overline{\kappa}_f \nabla_f^\delta \left(\tfrac{\delta_t}{\overline{S}_\star}\nabla_\star^\delta \cdot \left(\overline{S}_\star \left[h_\star^n\right]_\star \overline{u}_\star^{n+1}\right)\right) \\ &\qquad\qquad = -g\overline{\kappa}_f \nabla_f^\delta \left(h_\star^n + B_\star\right) \\ &h_k^{n+1} = h_k^n - \frac{\delta_t}{\overline{S}_k}\nabla_k^\delta \cdot \left(\overline{S}_\star \left[h_\star^n\right]_\star \overline{u}_\star^{n+1}\right) \end{aligned}$$

where $\mathscr{T}^f_{\mathbf{h}_\star,0}(V_\star) = -\frac{\overline{\kappa}_f}{[\mathbf{h}_\star]_f}\nabla_f^\delta\left(\frac{|\mathbf{h}_\star|^3}{3\overline{\kappa}_\star\overline{S}_\star}\nabla_\star^\delta\cdot\left(\overline{S}_\star V_\star\right)\right)$. This scheme is a first-order numerical scheme of $(DF_{h,0})$ and it adheres to the discrete energy dissipation law Proposition 5 with $\beta = 0$, implying in particular that $\mathscr{H}_f^{n+1} = 0$.

- When $\mu^2\varepsilon$ is negligible, the numerical scheme $(DF^{\mathrm{L}}_{h,B})$ tends to

$$(DF^{\mathrm{L}}_{D,B}) \qquad \begin{aligned} &\overline{u}_f^{n+1} + \mathscr{T}^f_{D_\star,B_\star}\left(\overline{u}_\star^{n+1}\right) - g\overline{\kappa}_f \nabla_f^\delta \left(\tfrac{\delta_t}{\overline{S}_\star}\nabla_\star^\delta \cdot \left(\overline{S}_\star \left[h_\star^n\right]_\star \overline{u}_\star^{n+1}\right)\right) \\ &\qquad\qquad = -g\overline{\kappa}_f \nabla_f^\delta \left(h_\star^n + B_\star\right) \\ &h_k^{n+1} = h_k^n - \frac{\delta_t}{\overline{S}_k}\nabla_k^\delta \cdot \left(\overline{S}_\star \left[h_\star^n\right]_\star \overline{u}_\star^{n+1}\right). \end{aligned}$$

This scheme is a first-order numerical scheme of $(DF_{D,B})$.

- When both $\mu^2\beta$ and $\mu^2\varepsilon$ are negligible, the numerical scheme $(DF^{\mathrm{L}}_{h,B})$ tends to

$$(DF^{\mathrm{L}}_{D,0}) \qquad \begin{aligned} &\overline{u}_f^{n+1} + \mathscr{T}^f_{D_\star,0}\left(\overline{u}_\star^{n+1}\right) - g\overline{\kappa}_f \nabla_f^\delta \left(\tfrac{\delta_t}{\overline{S}_\star}\nabla_\star^\delta \cdot \left(\overline{S}_\star \left[h_\star^n\right]_\star \overline{u}_\star^{n+1}\right)\right) \\ &\qquad\qquad = -g\overline{\kappa}_f \nabla_f^\delta \left(h_\star^n + B_\star\right) \\ &h_k^{n+1} = h_k^n - \frac{\delta_t}{\overline{S}_k}\nabla_k^\delta \cdot \left(\overline{S}_\star \left[h_\star^n\right]_\star \overline{u}_\star^{n+1}\right). \end{aligned}$$

This scheme is a first-order numerical scheme of $(DF_{D,0})$.

- When μ is negligible, all the schemes $(DF^{\mathrm{L}}_{h,B})$ $(DF^{\mathrm{L}}_{h,0})$, $(DF^{\mathrm{L}}_{D,B})$ and $(DF^{\mathrm{L}}_{D,0})$ tend to

$$(DF^{\mathrm{L}}_0) \qquad h_k^{n+1} - \frac{g\delta_t}{\overline{S}_k}\nabla_k^\delta \cdot \left(\overline{\kappa}_\star \overline{S}_\star \left[h_\star^n\right]_\star \nabla_\star^\delta \left(h_\star^{n+1} + B_\star\right)\right) = h_k^n.$$

This scheme is a first-order numerical scheme of $(DF_{D,B})$.

4.1.2 Fully implicit numerical scheme

In §4.1.1, it was highlighted that the semi-implicit scheme possesses first-order accuracy in time. To achieve a higher level of accuracy, a second-order version of this

scheme can be designed by employing a non-linear Crank-Nicolson scheme. We set

$$h_k^{n+1} = h_k^n - \frac{\delta_t}{\overline{S}_k}\nabla_k^\delta \cdot \left(\overline{S}_\star \left[h_\star^{[n+1/2]}\right]_\star \overline{u}_\star^{n+1/2}\right)$$
$$\overline{u}_f^{n+1/2} + \mu^2 \mathscr{T}^f_{h_\star^{[n+1/2]},B_\star}\left(\overline{u}_\star^{n+1/2}\right) = -g\overline{\kappa}_f \nabla_f^\delta \left(h_\star^{[n+1/2]} + B_\star\right)$$

where $h_k^{[n+1/2]} = \frac{h_\star^{n+1}+h_\star^n}{2}$ and the operator $\mathscr{T}^f_{\mathbf{h}_\star,\mathbf{b}_\star}$ is defined in (30). Given the non-linearity of the scheme ($DF^{\mathrm{NL}}_{h,B}$), it necessitates the use of a fixed-point method. While a Newton fixed point is a possibility, to extend the entropy stability Proposition 5, we employ a Picard fixed point that gives

$$(DF^{\mathrm{NL}}_{h,B}) \qquad \begin{aligned} &\overline{u}_f^{n+1/2} + \mu^2 \mathscr{T}^f_{h_\star^{[\frac{n,r}{2}]},B_\star}\left(\overline{u}_\star^{n+1/2,r+1}\right) \\ &\quad - g\overline{\kappa}_f \nabla_f^\delta \left(\frac{\delta_t}{2\overline{S}_k}\nabla_k^\delta \cdot \left(\overline{S}_\star \left[h_\star^{[\frac{n,r}{2}]}\right]_\star \overline{u}_\star^{n+1/2,r+1}\right)\right) \\ &\qquad = -g\overline{\kappa}_f \nabla_f^\delta \left(h_\star^n + B_\star\right) \\ &h_k^{n,r+1} = h_k^n - \frac{\delta_t}{\overline{S}_k}\nabla_k^\delta \cdot \left(\overline{S}_\star \left[h_\star^{[\frac{n,r}{2}]}\right]_\star \overline{u}_\star^{n+1/2,r+1}\right) \end{aligned}$$

In this scheme, $h_k^{[\frac{n,r}{2}]} = \frac{h_k^n + h_k^{n,r}}{2}$ where $h_k^{n,0} = h_k^n$ and $h_k^{n+1} = h_k^{n,r+1}$ upon convergence. In practice, convergence is determined when the L^∞-error, defined as $\max_{k\in\mathbb{T}} \left|h_k^{n,r+1} - h_k^{n,r}\right|$, falls below a specified tolerance τ.

Proposition 6. *Let h_k^n be the solution of the numerical scheme ($DF^{\mathrm{NL}}_{h,B}$). Then the discrete potential energy $\mathscr{E}_k(h) = g\overline{S}_k h\left(\frac{h}{2} + B_k\right)$ adheres to the following dissipation law*

$$\begin{aligned} &\mathscr{E}_k\left(h_k^{n,r+1}\right) + \delta_t \nabla_k \cdot \left(\mathscr{G}_\star^{n+1/2} + \mathscr{H}_\star^{n+1/2}\right) = \mathscr{E}_k\left(h_k^n\right) \\ &\quad - \delta_t \left(\left[\frac{\overline{S}_\star \left[h_\star^{[\frac{n,r}{2}]}\right]_\star}{\overline{\kappa}_\star}\left|\overline{u}_\star^{n+1/2,r+1}\right|^2\right]_k + \frac{\overline{S}_k h_k^{[\frac{n,r}{2}]}}{\overline{\kappa}_k}\left(\left|\overline{w}_k^{n+1/2,r+1}\right|^2 + \frac{\left|\widetilde{w}_k^{n+1/2,r+1}\right|^2}{12}\right)\right) \end{aligned}$$

where the numerical energy flux is given by

$$\mathscr{G}_f^{n+1/2} = \left(g\left[h_\star^{[\frac{n,r}{2}]}\right]_f \left[h_\star^{[\frac{n,r+1}{2}]} + B_\star\right]_f + \mu\left[h_\star^{[\frac{n,r}{2}]}\overline{q}_\star^{n+1/2,r+1}\right]_f\right)\overline{S}_f \overline{u}_f^{n+1/2,r+1}$$

and the error in the numerical flux is

$$\mathscr{H}_f^{n+1/2} = \mu\beta\frac{\delta_f^2}{4}\overline{S}_f \overline{u}_f^{n+1/2,r+1} \cdot \nabla_f^\delta B_\star \nabla_f^\delta q_{B,\star}^{n+1/2,r+1}.$$

Proof. Thanks to the Crank-Nicolson time scheme, the first step of the proof becomes an equality, i.e.

$$\begin{aligned} \mathscr{E}_k^{n+1} = \mathscr{E}_k^n &- \delta_t \nabla_k^\delta \cdot \left(g\left[h_\star^n\right]_\star \left[h_\star^{n+1} + B_\star\right]_\star \overline{S}_\star \overline{u}_\star^{n+1}\right) \\ &+ \delta_t g\left[\overline{S}_\star \left[h_\star^n\right]_\star \overline{u}_\star^{n+1} \cdot \nabla^\delta\left(h_\star^{n+1} + B_\star\right)\right]_k. \end{aligned}$$

The remainder of the proof follows that of Proposition 5. □

• When $\mu^2\beta$ is negligible, the numerical scheme ($DF^{\mathrm{NL}}_{h,B}$) tends to

$$(DF^{\mathrm{NL}}_{h,0})\qquad \begin{aligned} &\overline{u}_f^{n+\frac12} + \mu^2 \mathscr{T}^f_{h_\star^{[\frac{n,r}{2}]},0}\left(\overline{u}_\star^{n+\frac12,r+1}\right) \\ &\quad - g\overline{\kappa}_f \nabla_f^\delta\left(\frac{\delta_t}{2\overline{S}_k}\nabla_k^\delta\cdot\left(\overline{S}_\star\left[h_\star^{[\frac{n,r}{2}]}\right]_\star \overline{u}_\star^{n+\frac12,r+1}\right)\right) \\ &\qquad = -g\overline{\kappa}_f\nabla_f^\delta\left(h_\star^n + B_\star\right) \\ &h_k^{n,r+1} = h_k^n - \frac{\delta_t}{\overline{S}_k}\nabla_k^\delta\cdot\left(\overline{S}_\star\left[h_\star^{[\frac{n,r}{2}]}\right]_\star \overline{u}_\star^{n+\frac12,r+1}\right). \end{aligned}$$

This scheme is a second-order numerical scheme of ($DF_{h,0}$) and it adheres to the discrete energy dissipation law Proposition 5 with $\beta = 0$, implying in particular that $\mathscr{H}_f^{n+1} = 0$.

• When $\mu^2\varepsilon$ is negligible, the numerical scheme ($DF^{\mathrm{NL}}_{h,B}$) tends to

$$(DF^{\mathrm{NL}}_{D,B})\qquad \begin{aligned} &\overline{u}_f^{n+\frac12} + \mathscr{T}^f_{D_\star,B_\star}\left(\overline{u}_\star^{n+\frac12,r+1}\right) \\ &\quad - g\overline{\kappa}_f \nabla_f^\delta\left(\frac{\delta_t}{2\overline{S}_k}\nabla_k^\delta\cdot\left(\overline{S}_\star\left[h_\star^{[\frac{n,r}{2}]}\right]_\star \overline{u}_\star^{n+\frac12,r+1}\right)\right) \\ &\qquad = -g\overline{\kappa}_f\nabla_f^\delta\left(h_\star^n + B_\star\right) \\ &h_k^{n,r+1} = h_k^n - \frac{\delta_t}{\overline{S}_k}\nabla_k^\delta\cdot\left(\overline{S}_\star\left[h_\star^{[\frac{n,r}{2}]}\right]_\star \overline{u}_\star^{n+\frac12,r+1}\right). \end{aligned}$$

This scheme is a second-order numerical scheme of ($DF_{D,B}$)

• When both $\mu^2\beta$ and $\mu^2\varepsilon$ are negligible, the numerical scheme ($DF^{\mathrm{L}}_{h,B}$) tends to

$$(DF^{\mathrm{NL}}_{D,0})\qquad \begin{aligned} &\overline{u}_f^{n+\frac12} + \mathscr{T}^f_{D_\star,0}\left(\overline{u}_\star^{n+\frac12,r+1}\right) \\ &\quad - g\overline{\kappa}_f \nabla_f^\delta\left(\frac{\delta_t}{2\overline{S}_k}\nabla_k^\delta\cdot\left(\overline{S}_\star\left[h_\star^{[\frac{n,r}{2}]}\right]_\star \overline{u}_\star^{n+\frac12,r+1}\right)\right) \\ &\qquad = -g\overline{\kappa}_f\nabla_f^\delta\left(h_\star^n + B_\star\right) \\ &h_k^{n,r+1} = h_k^n - \frac{\delta_t}{\overline{S}_k}\nabla_k^\delta\cdot\left(\overline{S}_\star\left[h_\star^{[\frac{n,r}{2}]}\right]_\star \overline{u}_\star^{n+\frac12,r+1}\right). \end{aligned}$$

This scheme is a second-order numerical scheme of ($DF_{D,0}$)

• When both μ is negligible, all the schemes ($DF^{\mathrm{NL}}_{h,B}$) ($DF^{\mathrm{NL}}_{h,0}$), ($DF^{\mathrm{NL}}_{D,B}$) and ($DF^{\mathrm{NL}}_{D,0}$) tend to

$$(DF^{\mathrm{NL}}_{0})\qquad \begin{aligned} &h_k^{n,r+1} - \frac{g\delta_t}{2\overline{S}_k}\nabla_k^\delta\cdot\left(\overline{\kappa}_\star\overline{S}_\star\left[h_\star^{[\frac{n,r}{2}]}\right]_\star \nabla_\star^\delta\left(h_\star^{n,r+1} + B_\star\right)\right) \\ &\quad = h_k^n + \frac{g\delta_t}{2\overline{S}_k}\nabla_k^\delta\cdot\left(\overline{\kappa}_\star\overline{S}_\star\left[h_\star^{[\frac{n,r}{2}]}\right]_\star \nabla_\star^\delta\left(h_\star^n + B_\star\right)\right). \end{aligned}$$

This scheme is a second-order numerical scheme of (DF_0).

The advantage of ($DF^{\mathrm{L}}_{D,B}$) compared to ($DF^{\mathrm{L}}_{h,B}$) lies in the fact that a portion of the matrix, represented by $\mathcal{T}^{f}_{D_\star,B_\star}$, remains time-independent. Consequently, it does not need to be recomputed at every time step. For the scheme ($DF^{\mathrm{L}}_{h,0}$), the linear system is considerably simpler, leading to computational advantages. Similar benefits apply to the scheme ($DF^{\mathrm{L}}_{D,0}$) as well. These advantages extend to the non-linear schemes discussed in §4.1.2. In these cases, the computational gains become even more pronounced as they necessitate solving multiple linear systems at each time step.

4.2 Numerical results

To illustrate the solutions of the hydrodynamic models, we propose the following test case. We consider a one-dimensional computational domain $\Omega = [0,10]$ with a homogeneous mesh $\mathcal{T} = [1,N] \cap \mathbb{N}$ and a spatial step $\delta_x = \frac{10}{N}$. The substratum is defined by

$$B(x) = -1 + \beta \cos\left(\frac{7\pi x}{10}\right).$$

We impose wall boundaries condition by setting $\overline{u}(t,0) = \overline{u}(t,10) = 0$. The initial condition is given by

$$h^0(x) = 1 + \frac{\varepsilon}{2}\tanh\big(-50\mu(x-5)\big).$$

The parameters β, ε and μ are further defined to analyze the sensitivity of the solution to these parameters.

4.2.1 Sensitivity analysis of numerical parameters

Let's start our analysis by examining the behavior of the numerical scheme under the simplest conditions, characterized by a flat bedrock with parameters $\beta = 0$, $\varepsilon = 1$, and $\mu = 10^{-1}$. In Figure 4, we present the outcomes of the semi-implicit scheme ($DF^{\mathrm{L}}_{h,B}$) with a spatial discretization $\delta_x = 10^{-3}$ and varying time steps δ_t at three distinct times. For comparative purposes, both the initial condition and the solution computed with the hydrostatic model (DF^{L}_{0}) with $\delta_t = \delta_x$ are included.

A primary observation is the emergence of instabilities for large time steps, specifically when $\delta_t \geq 10^{-4}$. Importantly, these instabilities do not refute the findings of Proposition 5, which asserts the unconditional stability of the solution in the L^2-norm. The temporal evolution of the normalized energy $\frac{\mathscr{E}(t)}{\mathscr{E}(0)}$ is depicted in Figure 5. Consistent with Proposition 5, the energy is decreasing. Notably, at certain points in time, later for smaller time steps, the rate of energy decay decreases, leading to the emergence of instabilities. The origins of these instabilities remain unclear. To mitigate their occurrence, it would be beneficial to investigate stability within the context of Total Variation Diminishing (TVD) norms. However, this exploration presents challenges at both the discrete and continuous levels. Further insights from Figure 5 reveal that the energy decay rate is more gradual for the hydrodynamic model during the initial period. Moreover, Figure 4 highlights that pronounced gradients persist

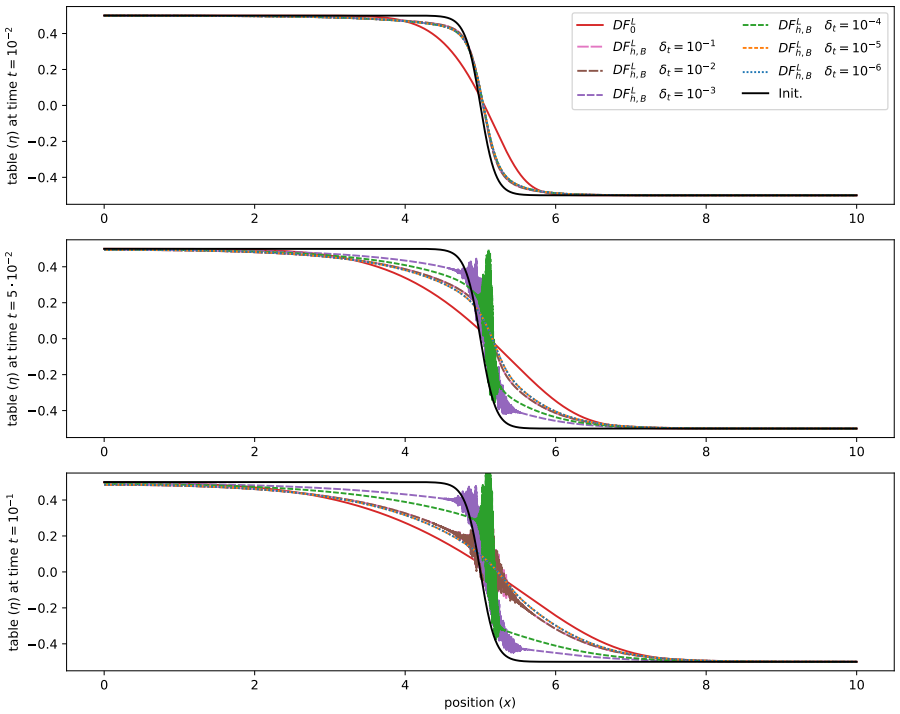

Figure 4: *§4.2.1* – Water table elevations computed using the semi-implicit scheme ($DF_{h,B}^{\mathrm{L}}$) with $\delta_x = 10^{-3}$, is plotted for varying time steps δ_t at $t = 10^{-2}$ (top line), $t = 5 \cdot 10^{-2}$ (middle line), and $t = 10^{-1}$ (bottom line). The initial condition is depicted in black, while the solution computed using the hydrostatic model (DF_0^{L}) with a time step $\delta_t = \delta_x$ is plotted in red.

for extended durations as suggest by the linear analysis §3.4. Nevertheless, over extended time intervals, the hydrodynamic solution eventually converges towards the hydrostatic solution.

In the simulations using the fully implicit scheme ($DF_{h,B}^{\mathrm{NL}}$), we encountered non-convergence issues when instabilities began to manifest. To address this issue, we implemented a time step limitation within the iterative process. Specifically, if the fixed-point iteration does not converge after $r_{\max}$ iterations, we reduce the time step by multiplying it with a factor $0 < \omega < 1$. At the start of a new time iteration, the time step is reset to its maximum value. For the simulations presented in this study, we chose $r_{\max} = 20$ and $\omega = 0.5$. In Figure 6, we display the outcomes of the fully implicit scheme ($DF_{h,B}^{\mathrm{NL}}$) with $\delta_x = 10^{-3}$ for various maximal time steps δ_t at three distinct times. The imposed time step limitation successfully keeps the practical time step approximately at $2 \cdot 10^{-4}$ for larger maximal time steps, which is consistent with

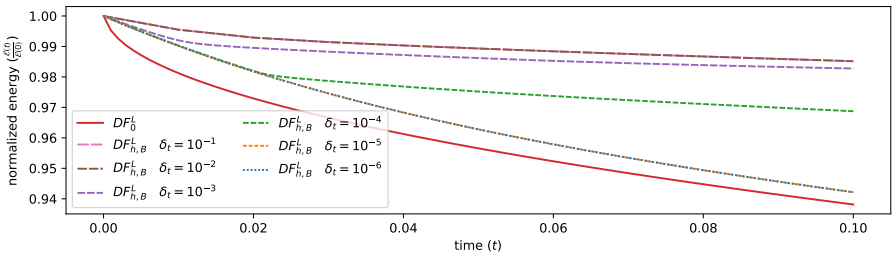

Figure 5: §4.2.1 – Temporal evolution of the normalized energy $\frac{\mathscr{E}(t)}{\mathscr{E}(0)}$, for the semi-implicit scheme ($DF^{\mathrm{L}}_{h,B}$) with $\mu = 10^{-1}$ and $\delta_x = 10^{-3}$, across various time steps δ_t, is depicted. Additionally, the energy profile for the hydrostatic model (DF^{L}_{0}) with a time step $\delta_t = \delta_x$ is illustrated in red.

our findings from the semi-implicit scheme ($DF^{\mathrm{L}}_{h,B}$). Consequently, the outcomes derived using various maximum time steps overlap.

In Figure 7, we present the results obtained from various schemes for different spatial step sizes δ_x. The semi-implicit scheme ($DF^{\mathrm{L}}_{h,B}$) is executed with a time step set at $\delta_t = 10^{-6}$. The fully-implicit scheme ($DF^{\mathrm{NL}}_{h,B}$) is executed with a maximum time step set at 10^{-1}, but reduced by the time step limitation process. In practice, the effective time step is approximately 10^{-1} for $\delta_x = 10^{-1}$, $5\cdot10^{-3}$ for $\delta_x = 10^{-2}$, and $2\cdot10^{-4}$ for $\delta_x = 10^{-3}$. Both hydrostatic schemes, (DF^{L}_{0}) and (DF^{NL}_{0}), are executed with $\delta_t = \delta_x$.

We observe that, except for the case with the coarse mesh $\delta_x = 10^{-1}$ computed with the fully-implicit scheme ($DF^{\mathrm{NL}}_{h,B}$), where the time step limitation is not triggered, the outcomes from the hydrodynamic models seem converged. With the coarse mesh, the results from the hydrodynamic scheme ($DF^{\mathrm{NL}}_{h,B}$) align with those of the hydrostatic scheme (DF^{NL}_{0}). This alignment suggests that numerical diffusion plays a more important role than hydrodynamic effects. This coarse result exhibits inflection points near strong gradients. This phenomenon is a well-documented characteristic of the Crank-Nicolson method when applied to diffusion equations, see [4]. It's noteworthy that the space step does not seem to have a significant impact on the results, which might seem counterintuitive given the presence of strong gradients. Specifically, the semi-implicit scheme ($DF^{\mathrm{L}}_{h,B}$) with $\delta_x = 10^{-1}$ and $\delta_t = 10^{-6}$ produces outcomes that align closely with the finer resolution using $\delta_x = 10^{-3}$.

4.2.2 Sensitivity analysis of physical parameters

We now shift our focus to examining the responses of the various models as the physical parameters undergo variations. For clarity and reduced spurious oscillations, we will exclusively present results using the semi-implicit scheme (DF^{L}_{0}) for the hydrostatic model and the fully-implicit scheme ($DF^{\mathrm{NL}}_{h,B}$) with the time step limitation process for the hydrodynamic model.

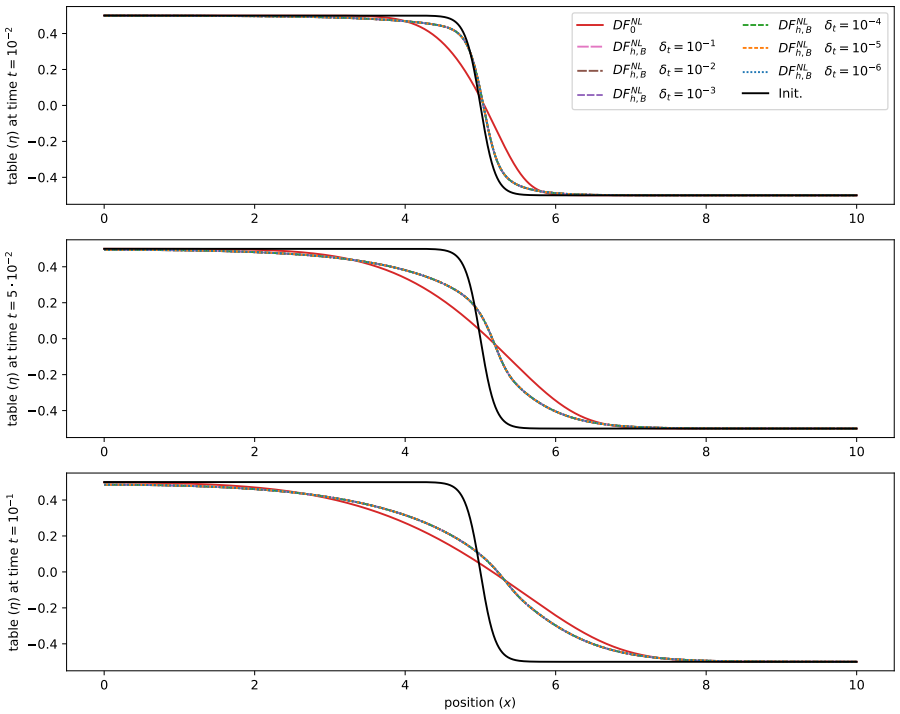

Figure 6: *§4.2.1* – Water table elevations computed using the fully-implicit scheme ($DF_{h,B}^{\mathrm{NL}}$) with $\delta_x = 10^{-3}$, is plotted for varying time steps δ_t at $t = 10^{-2}$ (top line), $t = 5 \cdot 10^{-2}$ (middle line), and $t = 10^{-1}$ (bottom line). The initial condition is depicted in black, while the solution computed using the hydrostatic model (DF_0^{NL}) with a time step $\delta_t = \delta_x$ is plotted in red.

On Figure 8, the results of the hydrostatic model (DF_0) and the hydrodynamic model ($DF_{h,B}$) are depicted for $\beta = 0$, $\varepsilon = 1$ and several values of μ. For sufficiently small μ values, the hydrodynamic model ($DF_{h,B}$) closely aligns with the hydrostatic model (DF_0). However, for larger μ values, the hydrodynamic model preserves the pronounced gradient of the water table for a longer duration, a behavior consistent with the linear analysis presented in §3.4. Specifically, for $\mu = 1$ (top line of Figure 8), we observe that the initial slope is mainly preserved, even as the amplitude of rapid variations in the water table diminishes. This results in a front that expands into regions with a lower water table level.

On Figure 9, the outcomes of the hydrostatic model (DF_0), the fully non-linear hydrodynamic model ($DF_{h,B}$), and the weakly non-linear hydrodynamic model ($DF_{D,B}$) are presented for $\beta = 0$, $\mu = 10^{-1}$, and various values of ε. For sufficiently small ε values, the weakly non-linear hydrodynamic model ($DF_{D,B}$) closely aligns with the

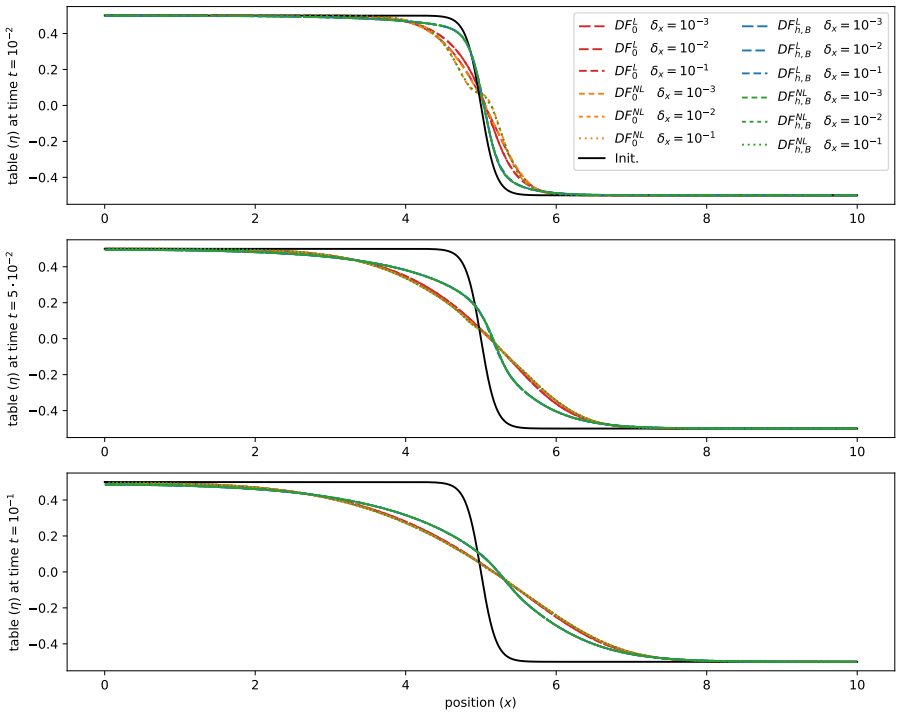

Figure 7: §4.2.1 – Water table elevations computed using the schemes ($DF_{h,B}^{\mathrm{L}}$), ($DF_{h,B}^{\mathrm{NL}}$), (DF_0^{L}), and (DF_0^{NL}) across various spatial step sizes: $\delta_x = 10^{-1}$, $\delta_x = 10^{-2}$ and $\delta_x = 10^{-3}$ at $t = 10^{-2}$ (top line), $t = 5 \cdot 10^{-2}$ (middle line), and $t = 10^{-1}$ (bottom line). The initial condition is depicted in black.

fully non-linear hydrodynamic model ($DF_{h,B}$). As ε approaches 1, distinctions between the two models become more noticeable. The divergence between the models becomes particularly pronounced when water depth is minimal (we recall that the substratum is located at $z = -1$), as depicted in the top line of Figure 9. Near dry regions, the solution from the weakly non-linear hydrodynamic model ($DF_{D,B}$) exhibits a steeper profile. Conversely, the fully non-linear hydrodynamic model ($DF_{h,B}$) encounters challenges in defining solutions within dry areas, where $h = 0$. While the weakly non-linear hydrodynamic model ($DF_{D,B}$) provides well-defined solutions in these regions, its applicability might be questionable.

On Figure 10, the results of the models (DF_0), ($DF_{h,B}$), ($DF_{D,B}$), ($DF_{h,0}$), and ($DF_{D,0}$) are displayed at time $t = 10^{-1}$, with $\mu = 10^{-1}$, $\varepsilon = 1$, and various values of β. Even for $\beta = 10^{-1}$, distinctions between the solutions obtained from the small bedrock models ($DF_{h,0}$) and ($DF_{D,0}$) and those from the arbitrary bedrock models ($DF_{h,B}$) and ($DF_{D,B}$) are evident. However, the overall solution behaviors remain

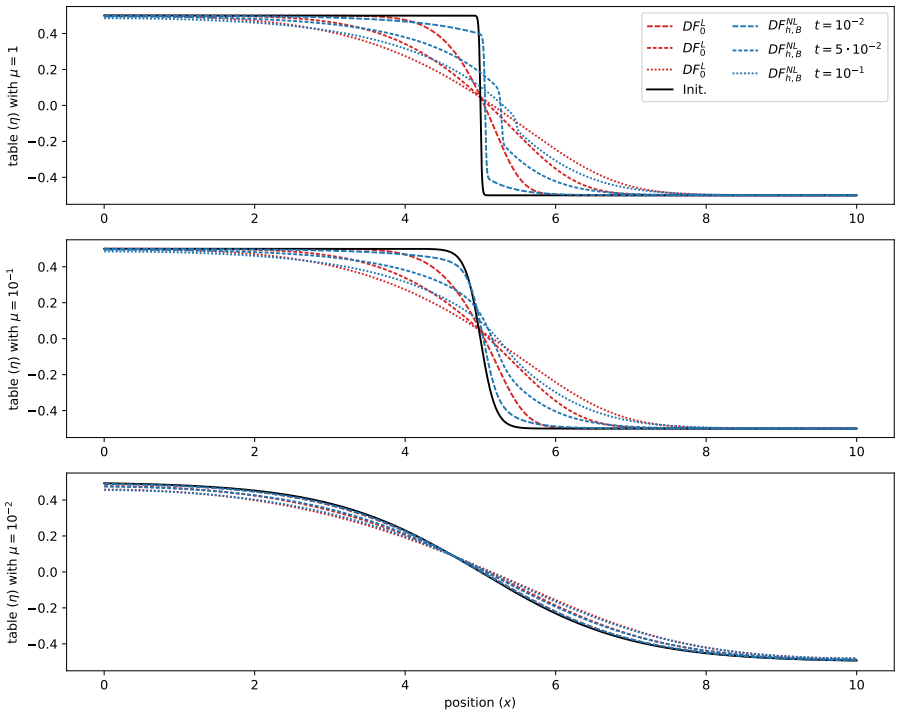

Figure 8: §4.2.2 – Water table elevations obtained by the hydrostatic model (DF_0) and the hydrodynamic model ($DF_{h,B}$) at $t = 10^{-2}$, $t = 5 \cdot 10^{-2}$ and $t = 10^{-1}$ for the parameters $\beta = 0$, $\varepsilon = 1$ and $\mu = 1$ (top line), $\mu = 10^{-1}$ (middle line) and $\mu = 10^{-2}$ (bottom line). The initial condition is depicted in black.

similar. For larger values of β, it is observed that the water table obtained with the small bedrock models ($DF_{h,0}$) and ($DF_{D,0}$) becomes non-monotonic, unlike the water table derived from the arbitrary bedrock models ($DF_{h,B}$) and ($DF_{D,B}$) (refer to $x \in [4,5]$ in the top line of Figure 10). Consistent with prior observations, the water table from the weakly non-linear models ($DF_{D,B}$) and ($DF_{D,0}$) exhibits steeper gradients when the water depth is minimal. However, in this scenario, it descends below the initial water table level, violating the maximum principle with weakly non-linear models ($DF_{D,B}$) and ($DF_{D,0}$). The maximum principle is well-known for the hydrostatic model (DF_0) but remains unproven for the hydrodynamic model ($DF_{h,B}$). It has been demonstrated for analogous linear equation see [15]. The applicability of this principle to its discrete counterpart remains an open question. However, the numerical simulation never violate the maximum principle with the hydrodynamic model ($DF_{h,B}$).

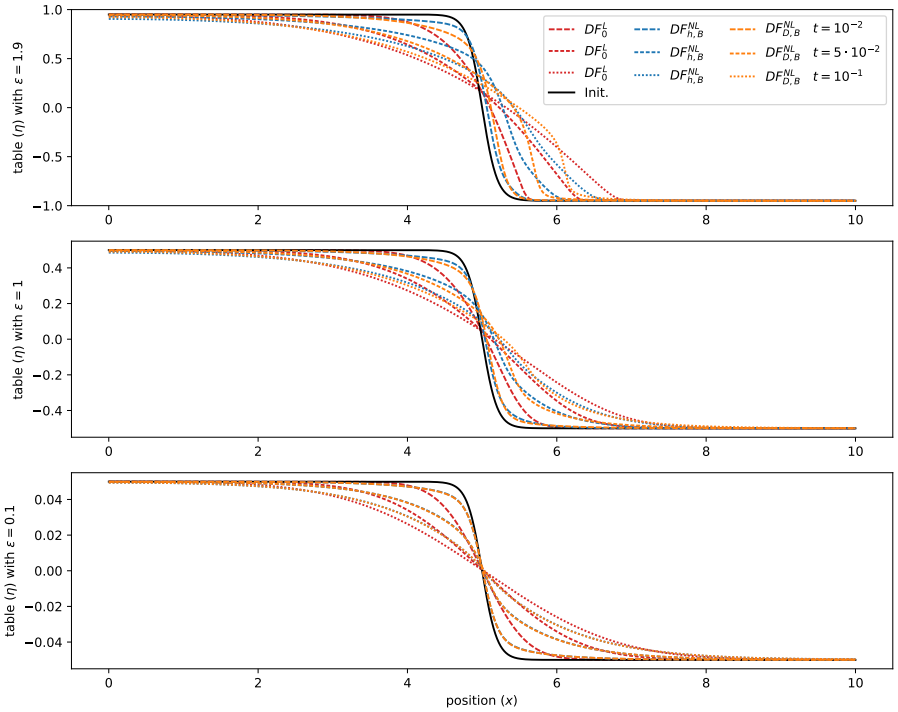

Figure 9: §4.2.2 – Water table elevation obtained with the models (DF_0), ($DF_{h,B}$) and ($DF_{D,B}$) at $t = 10^{-2}$, $t = 5 \cdot 10^{-2}$ and $t = 10^{-1}$ for the parameters $\beta = 0$, $\mu = 10^{-1}$ and $\varepsilon = 1.9$ (top line), $\varepsilon = 1$ (middle line) and $\varepsilon = 10^{-1}$ (bottom line). The initial condition is depicted in black.

5 Conclusion

In this study, we have developed a hierarchy of reduced models tailored for the groundwater wave problem within the Dupuit-Forchheimer regime, drawing parallels with the shallow water regime in water wave problems. This approach incorporates the first-order effects of hydrodynamic pressure. Our primary model in this hierarchy is both non-linear and non-local in nature. It is designed to accommodate arbitrary variations in both the water table and the bedrock, while also adhering to an energy dissipation law. Furthermore, we have crafted simplified versions of the model to cater to specific scenarios. In the regime characterized by minor variations in bedrock, the non-local operator is notably simplified. In the regime characterized by minor variations in water table, a linearization of the non-local operator can be reasonably used. To provide a comprehensive understanding of the solution behaviors exhibited by these models, we have conducted one-dimensional simulations, offering valuable insights into their performance and applicability.

While our numerical scheme successfully maintains energy dissipation at the

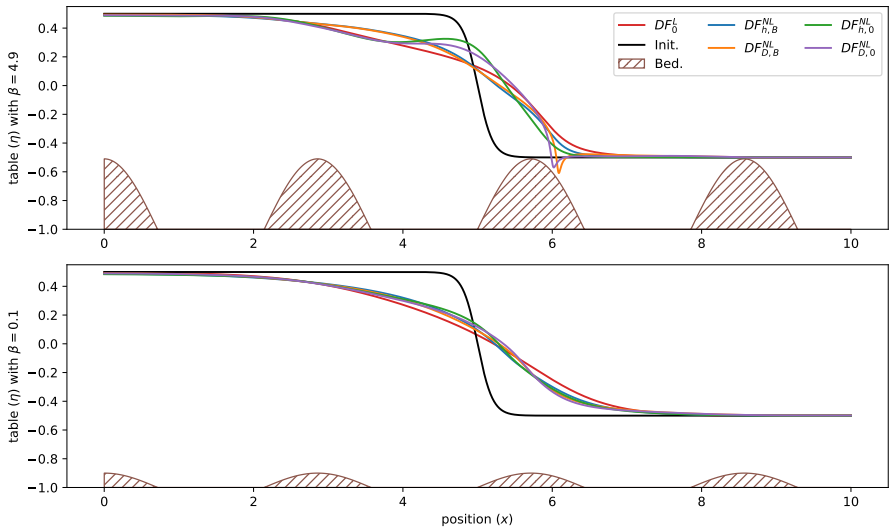

Figure 10: §4.2.2 – Water table elevation obtained with the models (DF_0), ($DF_{h,B}$), ($DF_{D,B}$), ($DF_{h,0}$) and ($DF_{D,0}$) at $t = 10^{-1}$ with $\mu = 10^{-1}$, $\varepsilon = 1$ and $\beta = 4.9$ (top line) and $\beta = 10^{-1}$ (bottom line). The initial condition is depicted in black.

discrete level without imposing constraints on the time step, it does exhibit spurious instabilities when subjected to excessively large time steps. The underlying causes of these instabilities remain elusive. A detailed analysis of solution regularity could offer valuable insights to enhance the robustness of our computational approach. Notably, numerical simulations indicate that the fully non-linear model, even when applied over intricate bedrock configurations, consistently preserves solution monotonicity over time. Preserving monotonicity at the discrete level can significantly enhance the robustness of numerical computations. However, it appears that the simplified models within our hierarchy do not maintain this property. Ensuring the robustness of our numerical strategy, particularly when dealing with large time steps, is imperative for applications that encompass expansive space and time scales. Also introducing an a posteriori estimator to facilitate the convergence of the non-linear problem could be a crucial advancement in this direction.

From a mathematical point of view, the derivation technics used in the reduction of water wave models, as presented in [22, 23], seems promising for justifying our groundwater wave reduced models, especially when considering constant permeability and porosity. Another logical progression of this research would involve exploring higher-order hydrodynamic models, akin to those proposed for water wave problems [19, 25, 26]. Natural porous media often consist of horizontal layers with varying compositions and properties. To address this complexity, a layerwise model, following [13], could be explored. Two significant challenges remain in this field that warrant attention. Firstly, boundary conditions, particularly Dirichlet conditions for water depth, need rigorous definition. This would not only validate the model but

also facilitate comparisons with analytical solutions and experimental data [8, 20]. Some recent advancements in dispersive free surface models might offer insights that are applicable to our context [24, 28]. Secondly, it's evident that hydrodynamic models are unsuitable in scenarios with discontinuous bottoms, unlike their hydrostatic counterparts. A potential solution could involve space coupling these two models, as previously demonstrated in related studies [16, 30]. Such integrative approaches could potentially overcome this limitation and enhance the applicability of the models in diverse real-world scenarios.

Acknowledgments

This research has been supported by the GeoFun project ANR-19-CE46-0010.

References

[1] AIRY, G. B. *Tides and waves.* B. Fellowes, 1845.

[2] ARNOLD, D., FALK, R., AND WINTHER, R. Finite element exterior calculus: from hodge theory to numerical stability. *Bulletin of the American mathematical society 47*, 2 (2010), 281–354.

[3] AUDUSSE, EMMANUEL, BOITTIN, LÉA, AND PARISOT, MARTIN. Asymptotic derivation and simulations of a non-local exner model in large viscosity regime. *ESAIM: M2AN 55*, 4 (2021), 1635–1668.

[4] BOLLEY, C., AND CROUZEIX, M. Conservation de la positivité lors de la discrétisation des problèmes d'évolution paraboliques. *RAIRO. Analyse numérique 12*, 3 (1978), 237–245.

[5] BOUWER, H. Limitation of the dupuit-forchheimer assumption in recharge and seepage. *Transactions of the ASAE 8*, 4 (1965), 512–0515.

[6] BRINKMAN, H. C. A calculation of the viscous force exerted by a flowing fluid on a dense swarm of particles. *Flow, Turbulence and Combustion 1*, 1 (Dec 1949), 27–34.

[7] BUCUR, C., VALDINOCI, E., ET AL. *Nonlocal diffusion and applications*, vol. 20. Springer, 2016.

[8] CASTRO-ORGAZ, O., GIRÁLDEZ, J. V., AND ROBINSON, N. I. Second-order two-dimensional solution for the drainage of recharge based on picard's iteration technique: A generalized dupuit-forchheimer equation. *Water Resources Research 48*, 6 (2012).

[9] DAGAN, G. Second order linearized theory of free-surface flow in porous media. *The Quarterly Journal of Mechanics and Applied Mathematics 20*, 4 (January 1967), 517–526.

[10] DE SAINT-VENANT, A.-J.-C. B. Théorie du mouvement non permanent des eaux, avec application aux crues des rivières et à l'introduction des marées dans leurs lits. *C.R. Acad. Sci. Paris 73* (1871), 147–154.

[11] DOMELEVO, K., AND OMNES, P. A finite volume method for the laplace equation on almost arbitrary two-dimensional grids. *ESAIM: Mathematical Modelling and Numerical Analysis 39*, 6 (Nov. 2005), 1203–1249.

[12] DUPUIT, J. É. J. *Études théoriques et pratiques sur le mouvement des eaux dans les canaux découverts et à travers les terrains perméables: avec des considérations relatives au régime des grandes eaux, au débouché à leur donner, et à la marche des alluvions dans les rivières à fond mobile.* Dunod, 1863.

[13] FERNÁNDEZ-NIETO, E. D., PARISOT, M., PENEL, Y., AND SAINTE-MARIE, J. A hierarchy of dispersive layer-averaged approximations of Euler equations for free surface flows. *Communications in Mathematical Sciences 16*, 5 (2018), 1169–1202.

[14] GOUDON, T., AND PARISOT, M. Non–local macroscopic models based on gaussian closures for the spizer-härm regime. *Kinetic and Related Models 4*, 3 (Aug 2011), 735–766.

[15] GOUDON, T., AND PARISOT, M. On the spitzer–härm regime and nonlocal approximations: Modeling, analysis, and numerical simulations. *Multiscale Modeling & Simulation 9*, 2 (2011), 568–600.

[16] GOUDON, T., AND PARISOT, M. Finite volume schemes on unstructured grids for non-local models: Application to the simulation of heat transport in plasmas. *Journal of Computational Physics 231*, 24 (2012), 8188 – 8208.

[17] HERMELINE, F. A finite volume method for the approximation of diffusion operators on distorted meshes. *Journal of Computational Physics 160*, 2 (2000), 481–499.

[18] KELLER, E. F., AND SEGEL, L. A. Traveling bands of chemotactic bacteria: A theoretical analysis. *Journal of Theoretical Biology 30*, 2 (1971), 235–248.

[19] KHORBATLY, B., ZAITER, I., AND ISRWAI, S. Derivation and well-posedness of the extended green-naghdi equations for flat bottoms with surface tension. *Journal of Mathematical Physics 59*, 7 (July 2018).

[20] KNIGHT, J. Improving the dupuit–forchheimer groundwater free surface approximation. *Advances in Water Resources 28*, 10 (2005), 1048–1056. Flow Processes in Hydrology: Contributions of J.-Y. Parlange.

[21] KROTKIEWSKI, M., LIGAARDEN, I. S., LIE, K.-A., AND SCHMID, D. W. On the importance of the stokes-brinkman equations for computing effective permeability in karst reservoirs. *Communications in Computational Physics 10*, 5 (2011), 1315–1332.

[22] LANNES, D. *The water waves problem: mathematical analysis and asymptotics*, vol. 188. Mathematical Surveys and Monographs, 2013.

[23] LANNES, D., AND BONNETON, P. Derivation of asymptotic two-dimensional time-dependent equations for surface water wave propagation. *Physics of Fluids 21*, 1 (2009).

[24] LANNES, D., AND WEYNANS, L. Generating boundary conditions for a boussinesq system. *Nonlinearity 33*, 12 (oct 2020), 6868–6889.

[25] MADSEN, P. A., AND SCHÄFFER, H. A. Higher–order boussinesq–type equations for surface gravity waves: derivation and analysis. *Philosophical Transactions of the Royal Society of London. Series A: Mathematical, Physical and Engineering Sciences 356*, 1749 (2022/03/16 1998), 3123–3181.

[26] MATSUNO, Y. Hamiltonian formulation of the extended green–naghdi equations. *Physica D: Nonlinear Phenomena 301-302* (2015), 1–7.

[27] NIELSEN, P., ASEERVATHAM, R., FENTON, J. D., AND PERROCHET, P. Groundwater waves in aquifers of intermediate depths. *Advances in Water Resources 20*, 1 (1997), 37–43.

[28] NOELLE, S., PARISOT, M., AND TSCHERPEL, T. A class of boundary conditions for time-discrete Green-Naghdi equations with bathymetry. *SIAM Journal on Numerical Analysis* (2022).

[29] P. SCHURTZ, G., NICOLAÏ, P., AND BUSQUET, M. A nonlocal electron conduction model for multidimensional radiation hydrodynamics codes. 4238–4249.

[30] PARISOT, M. Thick interfaces coupling technique for weakly dispersive models of waves. working paper or preprint, Feb. 2024.

[31] PATANKAR, S. *Numerical heat transfer and fluid flow*. CRC press, 2018.

[32] PATLAK, C. S. Random walk with persistence and external bias. *The bulletin of mathematical biophysics 15*, 3 (Sep 1953), 311–338.

[33] VAN SCHILFGAARDE, J. Limitations of dupuit-forchheimer theory in drainage. *Transactions of the ASAE 8*, 4 (1965), 515–0516.

[34] WESSELING, P. *Principles of computational fluid dynamics*, vol. 29. Springer Science & Business Media, 2009.

[35] ZERIHUN, Y. Extension of the Dupuit–Forchheimer Model for Non-Hydrostatic Flows in Unconfined Aquifers. *Fluids 3*, 2 (June 2018), 42.